

## Large-Scale, Low-Frequency Variability in Wind-Driven Ocean Gyres

PAVEL S. BERLOFF AND JAMES C. MCWILLIAMS

*Institute of Geophysics and Planetary Physics, University of California, Los Angeles, Los Angeles, California*

(Manuscript received 2 April 1998, in final form 16 November 1998)

### ABSTRACT

The authors investigate the spontaneous occurrence of large-scale, low-frequency variability of steadily forced, two-gyre, wind-driven circulations. The model dynamics is quasigeostrophic, the density stratification is represented in 1.5- and 2-layer approximations, and the wind stress pattern is either asymmetric or symmetric about the midbasin. The authors show that more generic variability arises when the forcing is strongly asymmetric, the Reynolds number is relatively large, and the baroclinic instability mechanism is active. The variability is explored for a wide range of values for the viscosity coefficient, that is, the Reynolds number. The regimes include steady circulation, periodic and quasiperiodic fluctuations near the beginning of the bifurcation tree, and chaotic circulations characterized by a broadband spectrum. Both the primary and secondary bifurcation modes and the spatiotemporal patterns within certain frequency bands in the chaotic regime are analyzed with an EOF decomposition combined with the time filtering.

In the symmetric case the 1.5-layer flow develops anomalously low-frequency fluctuations with a very non-Gaussian distribution. The baroclinic instability that arises in a 2-layer flow tends to weaken and regularize somewhat the low-frequency variability, but it still has the character of infrequent transitions between distinct gyre patterns. The variability of the circulation forced by asymmetric wind differs substantially from the symmetric forcing case. In 2-layer solutions the power at low frequencies progressively increases with the Reynolds number. The dominant low-frequency variability is associated with changes in the position and shape of the eastward jet and its associated western-basin recirculation zone. This variability occurs smoothly in time, albeit irregularly with a broadband spectrum.

### 1. Introduction

The wind-driven circulation in an enclosed, midlatitude basin is a classical problem in oceanography, and much previous attention has been given to its western boundary currents and mesoscale variability. Our focus is the large-scale, low-frequency intrinsic variability that develops at intermediate and large Reynolds number ( $Re$ ). In the introduction we pose the problem, give a brief review of the literature, and describe the model formulation. The results are split in sections 2 and 3, dealing with the asymmetrically and symmetrically forced circulations, respectively. The discussion and conclusions follow in section 4.

#### *a. Statement of the problem*

The spatiotemporal variability of the ocean may be roughly classified into three major categories: 1) the directly *forced* variability resulting from the slaved response of the ocean to time-dependent fluctuations of

the atmosphere, 2) the spontaneous variability that appears to be largely uncorrelated from fluctuations in the surface forcing (i.e., *intrinsic* variability), and 3) the intrinsically *coupled* variability of the combined ocean-atmosphere system, the most famous example of which is ENSO. We focus only on the intrinsic variability of the ocean by considering the situation where the wind forcing has no time dependence. We are primarily interested in the *large-scale, low-frequency* (LF) variations, which are loosely defined to be within a wide range of timescales from seasonal to interdecadal and length scales from the baroclinic deformation radius to the basin size.

We consider midlatitude, quasigeostrophic (QG) ocean dynamics with a prescribed density stratification in rectangular domain. For simplicity, the bottom topography, the coastal line geometry, and the thermal-haline forcing are excluded from the model. The primary questions that are posed and partially answered are the following:

- 1) What are the robust dynamical regimes of the circulation?
- 2) What are the important physical processes influencing these regimes?
- 3) How similar are the patterns at high  $Re$  to those near the beginning of the bifurcation tree?

---

*Corresponding author address:* Dr. Pavel S. Berloff, Institute of Geophysics and Planetary Physics, University of California, Los Angeles, Los Angeles, CA 90095.  
E-mail: pavel@atmos.ucla.edu

- 4) What are the generic spatiotemporal patterns corresponding to the LF variability of the flow?

To address these questions, we look at the spatiotemporal variability in 1.5- and 2-layer QG models. We consider two types of wind forcing: one symmetric with respect to the middle latitude and one asymmetric. In each situation we find solutions corresponding to early bifurcations of the flow at moderate  $Re$  as well as strongly chaotic solutions at significantly larger  $Re$ . The LF variability is analyzed by decomposing fluctuations of the complete and filtered solution fields into empirical orthogonal functions, EOFs (appendix A). Also, we analyze the time-mean circulation, the energy time series, and the energy conversions of the flow.

### b. Background

The theory and modeling of ocean gyres has been developed for several decades. Idealized basin geometries and wind patterns are often used with both single- and double-gyre circulations.

Holland (1978) and Haidvogel and Holland (1978) analyze the free-slip, QG, 2-layer, single- and double-gyre models with both horizontal and bottom friction. In their model the western boundary current separates and becomes an intense eastward jet (the “Gulf Stream”) with adjacent recirculation zones. Mesoscale eddies appear as a result of internal instabilities and interact with the time-mean flow transferring momentum from the upper to the lower layer.

The asymmetrically forced barotropic circulation with bottom friction (Harrison and Stalos 1982) has no intense eastward jet or recirculation. Instead, the western boundary current of the subtropical gyre intrudes deeply into the subpolar gyre, and the eastward jet develops a standing Rossby wave pattern. Moro (1988, 1990) extends this result by replacing bottom with lateral friction and finds that the steady state has a strongly meandering eastward jet surrounded by a large-scale vortex street. The vortex street becomes weaker as the forcing pattern approaches symmetry. The loss of stability by the asymmetric steady state is associated with vortex shedding from the entire vortex street. In a time-dependent, 3-layer model (Verron and LeProvost 1991), the street penetrates into the lower layer and becomes essentially barotropic, both in the time-mean and in the time-dependent fluctuations.

Multiple steady states are found for the barotropic, symmetrically forced, free-slip, QG problem in Cessi and Ierley (1995). Some of the steady states are perfectly symmetric and others appear in pairs due to the parity symmetry of QG dynamics. One of these pairs corresponds to the inertial runaway of the circulation (i.e., an extremely strong, basin-filling double gyre). Multiple steady states are also found in a barotropic, QG model with an alternative friction formulation (Primeau 1998) and in a shallow-water model (Speich et al. 1995) that

is equivalent to our 1.5-layer model in the QG approximation.

The time-dependent, barotropic circulation with bottom and biharmonic horizontal friction contains two major types of disturbances (LeProvost and Verron 1987): meandering of the eastward jet and radiation of Rossby wavelike features from the westward recirculation flow. The transient dynamics near the steady states found by Speich et al. (1995) is explored by Jiang et al. (1995): there the periodic solution arises from the steady state by a Hopf bifurcation and is characterized by the appearance and nonlinear interaction of multipole vortices with the eastward jet and each other. When the  $Re$  is further increased, the fluctuations become aperiodic. The circulation in a 1.5-layer, free-slip, QG model with “bottom” (i.e., interfacial) and biharmonic horizontal friction has multiple persistent flow patterns (i.e., preferred states) distinguished by their energy level and gyre shape (McCalpin and Haidvogel 1997). Transitions between these states are responsible for the LF variability. The high-energy state is associated with deep eastward penetration and weak meandering of the eastward jet. The low-energy state is associated with destruction of the jet and an intense generation of mesoscale eddies. It corresponds to the weakly unstable steady state of the system (Primeau 1998).

The lateral boundary condition influence is examined in Haidvogel et al. (1992). In this case, a 3-layer ocean is damped by both lateral and bottom friction, and the wall boundary condition is partial-slip governed by a parameter  $\alpha$ . The limit  $\alpha \rightarrow 0$  corresponds to free-slip and  $\alpha \rightarrow \infty$  to no-slip condition. The time-mean flow changes significantly when  $\alpha$  is increased. The separation points of the western boundary currents retreat in the subpolar and subtropical gyres (yielding two distinct eastward jets), the energy decreases significantly, and bottom dissipation is replaced by lateral friction as the main kinetic energy dissipator.

The most unstable eigenmodes near the primary bifurcation of the symmetric, 1.5-layer, partial-slip ( $\alpha = 1$ ), QG double gyre are of two types. One type, with an intermonthly period, is related to the resting-state basin modes in inviscid linear theory. The other type, with an interannual period, is associated with destabilization of the recirculations. The analogous eigenmode pair from the 2-layer model has a nearly annual period. The instability type for these modes is essentially baroclinic (Dijkstra and Katsman 1999, hereafter DK).

The dynamics of a single gyre is qualitatively similar to a double gyre. The mapping of the steady states, the stability, and the low-dimensional time-dependent behavior are analyzed in Sheremet et al. (1997) and Meacham and Berloff (1997a,b) for the barotropic model and in Berloff and Meacham (1997, 1998; hereafter BM1, BM2) for the 1.5- and 2-layer models. For a wide range of parameters, the large-time asymptotic regimes of the circulation correspond to low-dimensional attractors in the phase space. The typical low-dimensional

attractors are fixed points (steady states), limit cycles (periodic), tori (quasiperiodic), and strange attractors (chaotic). The generic bifurcation sequences consist of successive Hopf bifurcations with occasional period doublings. Multiple attractor branches are also found. The bifurcations are due to internal instabilities of the flow and may be of several types, including modes trapped in the vicinity of boundary currents, recirculations, and meanders. Also, there are modes resonant with the resting-state basin modes.

The evolution of the chaotic attractor at larger  $Re$  is not yet understood. On the one hand, the attractor dimension has a tendency to grow as  $Re$  increases, but reverse bifurcations occasionally reduce the dimension (BM1, BM2). Also, the number of attractors increases with  $Re$  (BM2). Therefore, it seems that the evolution of any attractors at high  $Re$  is a very complex process that may be almost intractable in a mathematically rigorous way. The key mathematical issue here is to reduce the initial large-dimensional model to a finite set of ODEs completely describing the motion on an *inertial manifold* (e.g., Constantin et al. 1989), but this seems to be very difficult. Another problem arises when the dimension is too large; identifying such an attractor requires very extensive computing (to our knowledge the largest reliable dimension estimate of 12 is in Guckenheimer and Buzyna 1983). For these reasons we will follow a more descriptive, experimental path in our analyses below.

The horizontal and vertical resolution sensitivity of the free-slip, QG model is such that the fine resolution increases the eastward jet penetration, downward eddy momentum flux, eddy energy, and time-mean eddy fluxes (i.e., rectification). The intermediate baroclinic modes (the second and third), despite their low kinetic energy level, are strongly involved in the eddy energy fluxes. However, the contribution from higher modes is negligible so the vertical resolution may be limited to a small number of modes (Barnier et al. 1991). In our solutions we increase the horizontal resolution with  $Re$  but hold the vertical resolution fixed at 1.5- and 2-layers. Also, for each solution we check that it does not change qualitatively when the number of grid points is doubled in each direction.

### c. Models

The QG potential vorticity equations (Pedlosky 1987) are solved in a square basin with size  $L$ . The equations for  $N$  active layers are

$$\frac{\partial \zeta_i}{\partial t} + J(\psi_i, \zeta_i) + \beta \frac{\partial \psi_i}{\partial x} = \frac{\delta_{i,1}}{\rho_1 H_1} \nabla \times \tau + \nu \nabla^4 \psi_i, \quad (1)$$

where  $\delta_{i,j} = 1$ , if  $i = j$ , and  $\delta_{i,j} = 0$ , if  $i \neq j$ , and  $i$  is the layer index starting from the top. The friction is only horizontal with  $\nu$  the eddy viscosity. The wind forcing

$$\frac{\delta_{i,1}}{\rho_1 H_1} \nabla \times \tau$$

acts only in the upper layer (all other layers are driven by pressure forces associated with time-dependent perturbations). The wind stress is zonal and has a two-gyre structure with an asymmetric component controlled by the parameter  $\lambda$ :

$$\tau(y) = \tau_0 \left[ \cos\left(\frac{2\pi y}{L}\right) + \lambda \sin\left(\frac{\pi y}{L}\right) \right]. \quad (2)$$

The parameter values are the following: the basin size is  $L = 3840$  km; the midbasin Coriolis parameter is  $f_0 = 0.83 \times 10^{-4} \text{ s}^{-1}$  with meridional gradient  $\beta = 2 \times 10^{-11} \text{ m}^{-1} \text{ s}^{-1}$ ; the layer depths are  $H_1 = 300$  m and  $H_2 = 3700$  m; and  $\tau_0 = 0.05 \text{ N m}^{-2}$ . We define the Reynolds number

$$Re = \frac{UL}{\nu},$$

where  $U = \tau_0(\rho_1 H_1 L \beta)^{-1}$  is the velocity scale from the Sverdrup balance. Other important nondimensional parameters are the viscous (Munk) length scale

$$\delta_M = \left(\frac{\nu}{\beta}\right)^{1/3}$$

and the inertial length scale

$$\delta_i = \left(\frac{U}{\beta}\right)^{1/2}.$$

We vary  $\nu$  from 400 to 1600  $\text{m}^2 \text{ s}^{-1}$ , while keeping  $\tau_0$  constant. This corresponds to  $\delta_M$  varying from 27.1 to 43.1 km, and  $\delta_i$  fixed at 10.85 km. The Reynolds number  $Re$  varies from 5.2 to 20.8.

Potential vorticity anomalies  $\zeta_i$  are connected with  $\psi_i$  through coupled elliptic equations

$$\nabla^2 \psi_i - (1 - \delta_{i,1}) S_{i,1} (\psi_i - \psi_{i-1}) - (1 - \delta_{i,N}) S_{i,2} (\psi_i - \psi_{i+1}) = \zeta_i, \quad (3)$$

where

$$S_{i,1} = f_0^2 \left( H_i g \frac{(\rho_i - \rho_{i-1})}{\rho_1} \right)^{-1},$$

$$S_{i,2} = f_0^2 \left( H_i g \frac{(\rho_{i+1} - \rho_i)}{\rho_1} \right)^{-1}$$

are the stratification parameters and  $\rho_i$  is the fluid density in the  $i$ th layer. The stratification is such that the baroclinic deformation radius for the 2-layer approximation, defined as

$$R_d = \sqrt{g \frac{(\rho_2 - \rho_1)}{\rho_1} \frac{1}{f_0} \sqrt{\frac{S_{1,2} H_1}{S_{1,2} + S_{2,1}}}},$$

is 52 km in most cases, with modest explorations in the

TABLE 1. 1.5-layer model runs with asymmetric ( $\lambda = 2$ ) forcing.

$\nu$	Character	I (%)	Comments (days)
1600	Steady state		
1400	Limit cycle	0.0	PM (221)
1100	Quasiperiodic	51.3	PM (200), SM (1400)
800	Chaotic	36.7	BB ( $\approx 270$ ); collection of spikes at LF
600	Chaotic	55.9	BB ( $\approx 310$ ); power build-up at LF
400	Chaotic	44.4	BB ( $\approx 420$ ); power build-up at LF

range of 40 to 65 km. The lateral boundary conditions are of no normal flow,

$$\psi_i|_C = \Gamma_i(t), \quad (4)$$

and no-slip,

$$\left. \frac{\partial \psi_i}{\partial n} \right|_C = 0. \quad (5)$$

The mass conservation constraint for each layer (McWilliams 1977) is

$$\frac{\partial}{\partial t} \iint_A \psi_i(x, y) dx dy = 0. \quad (6)$$

Here  $C$  is the bounding contour of the basin with area  $A$ . The governing equations (1), (2) were solved in dimensional form (SI units). The equations (1) are discretized using second-order finite differences on a uniform grid and are solved numerically using the boundary conditions (4)–(5) and the mass constraint (6). The elliptic problem (3) is solved by a direct method. The numerical model described here is similar to that used by Holland (1978). We vary the grid resolution with  $\nu$  so that the viscous scale  $\delta_M$  is adequately resolved, and the system of the governing equations (1) is well approximated.

We solve the equations (1) in 1.5- and 2-layer configurations. In the former case, the deep layer is assumed to be infinitely deep and resting; therefore, the circulation contains only the first-baroclinic vertical mode. In the latter case, both the barotropic and the first-baroclinic modes are present. The convergence of solutions with increased vertical resolution is an important issue, but we do not attempt to resolve it here.

## 2. Asymmetric forcing

### a. The 1.5-layer model

We choose  $\lambda = 2$ , which implies a much greater degree of asymmetry than in McCalpin and Haidvogel (1997). Using several values of  $\nu$ , we perform the six runs listed in Table 1. There the solution behavior is described using the following abbreviations: PM—primary mode, SM—secondary mode, and BB—broad band of a power spectrum. The corresponding time-scales (in days) are shown in brackets. The frequency content of the spectrum is partitioned into three bands:  $\omega < 0.58 \text{ yr}^{-1}$  (interannual band,  $I$ , with periods longer

than 630 days),  $0.58 \text{ yr}^{-1} \leq \omega \leq 1.74 \text{ yr}^{-1}$  (quasi-annual band,  $Q$ , with periods between 210 and 630 days), and  $1.74 \text{ yr}^{-1} < \omega$  (mesoscale band,  $M$ , with periods shorter than 210 days). The grid resolution is 15 km for  $\nu = 600$  and  $400 \text{ m}^2 \text{ s}^{-1}$ . It is 30 km for other values of  $\nu$ . The model is integrated forward in time until the solution converges to an attractor. Each attractor is identified from the total energy density time series,

$$E(t) = \frac{1}{A} \iint_A \sum_{i=1,2} \frac{H_i}{H} \frac{|\nabla \psi_i|^2}{2} + \frac{S_{1,2} H_1 + S_{2,1} H_2}{4(H_1 + H_2)} (\psi_1 - \psi_2)^2 dx dy, \quad (7)$$

as in BM1.

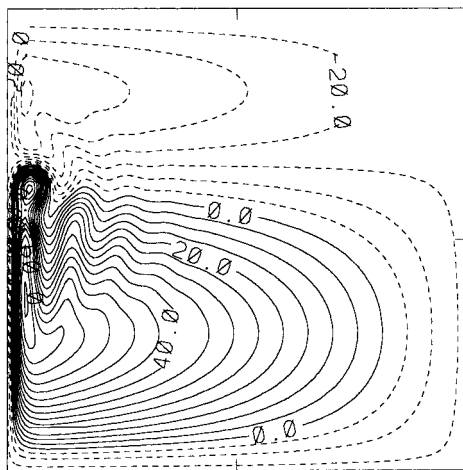
The stable steady state is found for  $\nu = 1600 \text{ m}^2 \text{ s}^{-1}$ . For  $\nu$ , between 1400 and  $1600 \text{ m}^2 \text{ s}^{-1}$ , the circulation loses stability due to the primary Hopf bifurcation (e.g., DK). The bifurcation destabilizes the steady state, and the limit cycle appears.

### 1) NONCHAOTIC ATTRACTORS

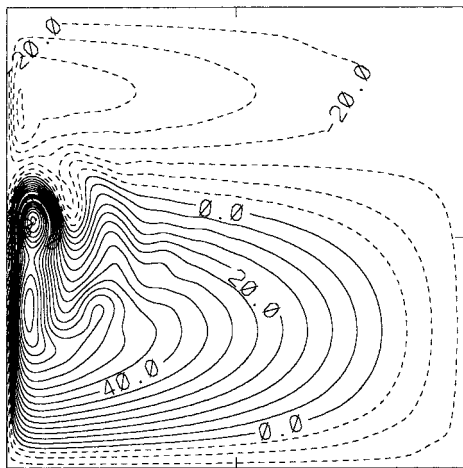
We find a periodic solution at  $\nu = 1400 \text{ m}^2 \text{ s}^{-1}$ . The time-mean  $\langle \psi_1 \rangle$  of this solution (Fig. 1a) consists of a weak subpolar and strong subtropical gyre. The mean flow contains the inertial recirculation and to the east of it is the spatially decaying oscillation (Cessi 1991). The oscillation has a period of 221 days, with strong disturbances in the northwestern part of the subtropical gyre and weak westward propagating waves in the interior of the basin. Following BM1, we iteratively reduce the most unstable eigenmode of a slightly supercritical steady state. The fluctuating circulation pattern associated with the limit cycle resembles the most unstable linear eigenmode of the nearby unstable steady state (Speich et al. 1995; Sheremet et al. 1997). This pattern occurs because the growing eigenmode's amplitude saturates by nonlinearity. The energy conversion density,  $P(x, y)$  (see appendix B), is mostly confined to the standing wave region and the adjacent recirculation zone (BM1).

The interior wave may be compared with inviscid linear basin modes of the resting fluid (Pedlosky 1987) that are governed by the dispersion relationship

$$T = \frac{4\pi^2}{\beta L} \left( m^2 + n^2 + \left( \frac{L}{\pi R d} \right)^2 \right)^{1/2}, \quad m = 1, 2, 3, \dots; \quad n = 1, 2, 3, \dots \quad (8)$$



(a)



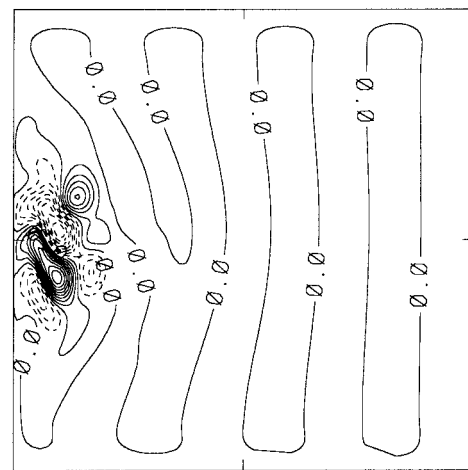
(b)

FIG. 1. The time-mean 1.5-layer circulation with  $\lambda = 2$  ( $CI = 5 \times 10^3$ ): (a)  $\nu = 1400 \text{ m}^2 \text{ s}^{-1}$ , (b)  $\nu = 400 \text{ m}^2 \text{ s}^{-1}$ .

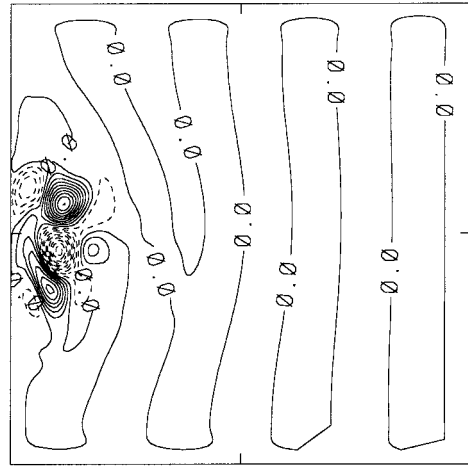
The basin mode with  $m = 8$  and  $n = 1$  (fit to the interior wave pattern) has the period of 148 days, which is substantially shorter than that of the limit cycle. On the other hand, the basin mode with period of the limit cycle has a rather small spatial scale and, therefore, is substantially damped by friction. Thus, we conclude that the interior wave pattern is not a basin mode. In contrast, a destabilized basin mode does occur in smaller basins (e.g., Sheremet et al. 1997; Meacham and Berloff 1997b; and DK). On the other hand, unbounded linear baroclinic Rossby wave governed by the dispersion relationship

$$T = \frac{2\pi}{\beta k_x} (k_x^2 + k_y^2 + Rd^{-2}) \quad (9)$$

has the period of 229 days for  $k_x = 8\pi/L$  and  $k_y = \pi/L$ , which is only slightly smaller than that of the limit cycle. Our interpretation of this is that the Rossby wave propagation mechanism is relevant to the dynamics of the



(a)



(b)

FIG. 2. The EOF pair representation of the periodic solution for 1.5-layers,  $\lambda = 2$ , and  $\nu = 1400 \text{ m}^2 \text{ s}^{-1}$ . Modes (a) and (b) have 53% and 46% of the variance, respectively ( $CI = 0.02$ ).

limit cycle, although it is not essential to its occurrence or its spatial pattern.

We perform an EOF analysis (see appendix A) for the limit cycle after bandpassing the solution around the dominant period of  $T = 221$  days (the bandpassing removes nonlinearly generated superharmonics). This decomposes the periodic fluctuation into two spatial modes with periodic temporal coefficients (Fig. 2), with variances of 53% and 46%, respectively. The temporal coefficients are in quadrature, with the first one leading the second by about 60 days. Thus, this EOF pair is a compact and convenient representation of the periodic propagating pattern of the limit cycle.

The circulation converges to quasiperiodic motion on a torus at  $\nu = 1100 \text{ m}^2 \text{ s}^{-1}$ . The energy spectrum (Fig. 3a) has two dominant spikes: one at about 200 days ( $\omega = 1.82 \text{ yr}^{-1}$ ), which can be traced to the primary Hopf bifurcation, and the other at about 1400 days ( $\omega = 0.26 \text{ yr}^{-1}$ ). The rest of the power is in the cross-harmonics

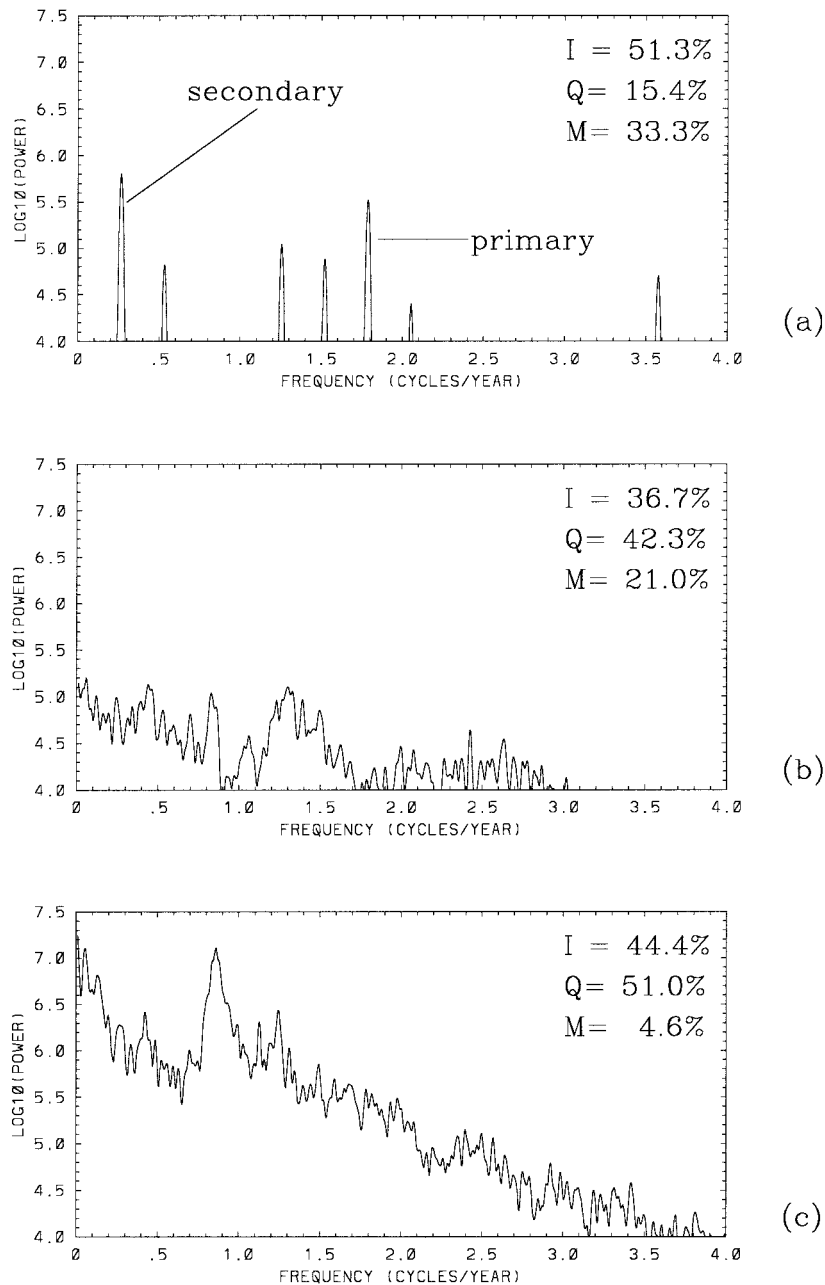


FIG. 3. Energy spectra for 1.5-layer solutions with  $\lambda = 2$ : (a)  $\nu = 1100 \text{ m}^2 \text{ s}^{-1}$ , (b)  $\nu = 800 \text{ m}^2 \text{ s}^{-1}$ , and (c)  $\nu = 400 \text{ m}^2 \text{ s}^{-1}$ .

and superharmonics of the dominant spikes. The second spike appears due to the internal instability and consequent Hopf bifurcation of the limit cycle. The secondary bifurcation mode may be a second unstable linear eigenmode of the underlying steady or time-average state (e.g., as in DK).

We also bandpass the solution around the secondary bifurcation frequency and decompose it in EOFs; the leading EOF pair is an approximation to the secondary bifurcation mode (Fig. 4). These EOFs contain 74% and

23% of the variance and are in quadrature with a time lag of about 700 days. This secondary mode has a fluctuation envelope surrounding the standing Rossby wave, with westward propagation within the envelope. In contrast to the primary mode, there is no Rossby wave pattern in the basin interior. This is because an unbounded linear baroclinic Rossby wave relation (11), with a 1400-day period, has one solution with the wavelength larger than  $L$ , which is too large a scale to resonate with the local instability pattern around the stand-

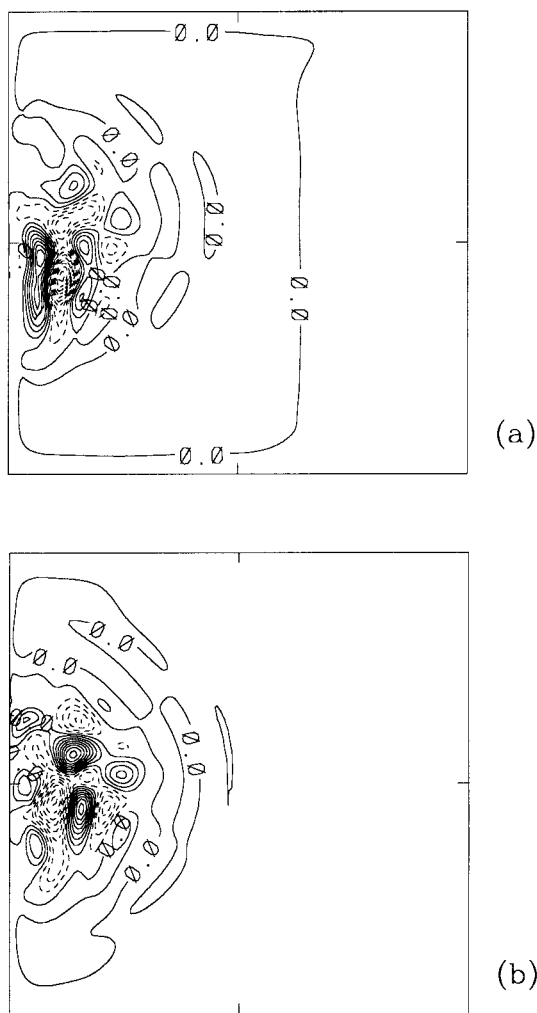


FIG. 4. EOF pair representing the secondary bifurcation mode for 1.5-layers,  $\lambda = 2$ , and  $\nu = 1100 \text{ m}^2 \text{ s}^{-1}$ . Modes (a) and (b) have 73% and 23% of the variance, respectively (CI = 0.02).

ing wave, and the other solution with very short scale, which is therefore damped by friction. Furthermore, a basin mode with an interannual period has too short a length scale and is strongly damped by friction as well.

## 2) CIRCULATION AT HIGH RE

At  $\nu = 800, 600$ , and  $400 \text{ m}^2 \text{ s}^{-1}$ , we see chaotic fluctuations with presumably large attractor dimension. The energy spectrum at  $\nu = 800 \text{ m}^2 \text{ s}^{-1}$  (Fig. 3b) is dominated by a set of intermonthly spikes around  $\omega \approx 1.34 \text{ yr}^{-1}$  and by a few spikes at lower frequencies; the partition among bands is  $I = 37\%$ ,  $Q = 42\%$ , and  $M = 21\%$ . The spectrum at  $\nu = 600 \text{ m}^2 \text{ s}^{-1}$  is qualitatively similar, but the power shifts to the interannual band:  $I = 56\%$ ,  $Q = 35\%$ , and  $M = 9\%$ . A similar buildup of LF power occurs in 3-layer double-gyre (Haidvogel et al. 1992) and 1.5-layer single-gyre (BM1) models.

In the time-average circulation at  $\nu = 400 \text{ m}^2 \text{ s}^{-1}$  (Fig. 1b), the main meander is weaker than at  $\nu = 1100 \text{ m}^2 \text{ s}^{-1}$  (Fig. 1a) and the currents are wider. The energy spectrum is characterized by a single, broad, dominant peak at  $\omega \approx 0.87 \text{ yr}^{-1}$  (a period of 420 days). This  $Q$ -band peak occurs around the same frequency in both the kinetic energy (KE) and the potential energy (PE) spectra, (unlike the 2-layer case; see section 2b). The power in the  $I$  band is mainly due to the PE contribution, with its maximum near  $\omega \approx 0.06 \text{ yr}^{-1}$ .

For the energy time series, we calculate the relative rms,

$$D = \frac{\sqrt{\langle (E - \langle E \rangle)^2 \rangle}}{\langle E \rangle}, \quad (10a)$$

skewness,

$$S = \frac{\langle (E - \langle E \rangle)^3 \rangle}{\langle (E - \langle E \rangle)^2 \rangle^{3/2}}, \quad (10b)$$

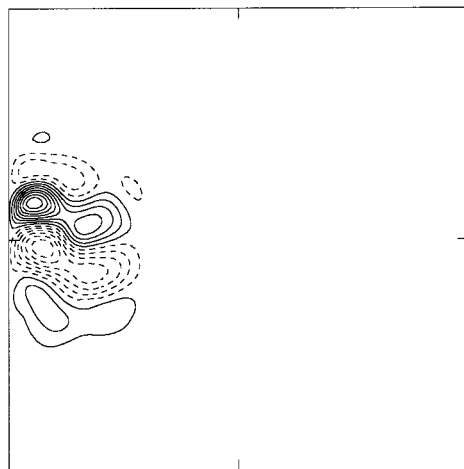
and flatness,

$$K = \frac{\langle (E - \langle E \rangle)^4 \rangle}{\langle (E - \langle E \rangle)^2 \rangle^2} - 3, \quad (10c)$$

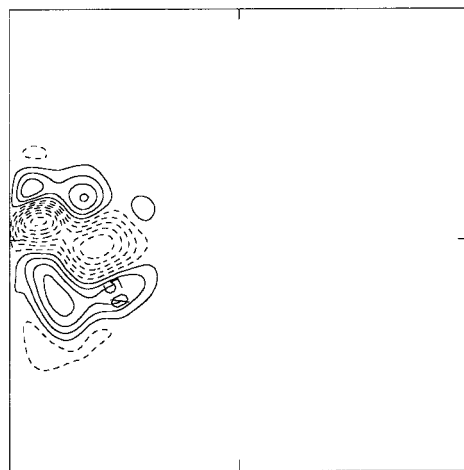
and compare the latter two with the corresponding moments of a normal (Gaussian) distribution (i.e., zero for each). The values at  $\nu = 400 \text{ m}^2 \text{ s}^{-1}$  are  $D = 0.052$ ,  $S = 0.11$ , and  $K = -0.27$ , which are not far from normal. Thus, this LF variability is not intermittent.

At  $\nu = 400 \text{ m}^2 \text{ s}^{-1}$ , we make an EOF decomposition for both the  $I$  band ( $\omega < 0.58 \text{ yr}^{-1}$ ) and the peak in the  $Q$  band ( $0.70 < \omega < 1.0 \text{ yr}^{-1}$ ). In both cases EOFs have a spatial scale larger than that of the early bifurcation modes. The leading pair of lowpass EOFs (Fig. 5) has variance fractions of 28% and 20%. These EOFs have anomalies corresponding to either intensification or meridional displacement of the eastward current and its recirculation zones. The time-lag correlation between the EOF coefficients has a rather weak maximum (about 0.2), and it corresponds to a cyclonic rotation of anomalies. The third and fourth EOFs are qualitatively similar to the leading pair and together contain an additional 22% of the total variance.

The temporal coefficients of the leading pair of  $Q$ -band EOFs (Fig. 6) have a strong quadrature relation (unlike the  $I$ -band EOF pair) and contain more than half of the total energy. The anomalies are near the eastward jet, suggesting that the quasi-annual variability may be associated with local instabilities in this region. Compared to the primary bifurcation mode, this EOF pair has larger horizontal and temporal scales. This is consistent with the fact that the eastward jet has a larger scale and presumably supports larger-scale instabilities. An important question is whether it is possible to follow a continuous evolution of an early bifurcation mode from low to high Re. From the preceding evidence, it seems plausible that the quasi-annual pattern at  $\nu = 400 \text{ m}^2 \text{ s}^{-1}$  and the primary bifurcation mode are dynamical



(a)



(b)

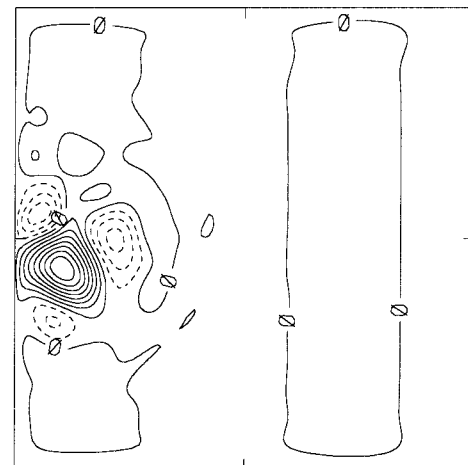
FIG. 5. EOFs for the low-passed solution with 1.5-layers,  $\lambda = 2$ , and  $\nu = 400 \text{ m}^2 \text{ s}^{-1}$ . The leading modes (a) and (b) have 28% and 20% of the variance, respectively (CI = 0.02).

cally related. The third EOF (with 11% of the variance) is similar to the *I*-band spatial pattern, and it may be due to a significant nonlinear interaction between the *I* and *Q* bands.

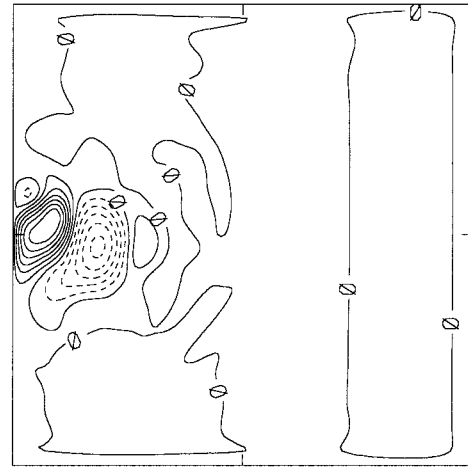
We explore the dependence of the circulation at  $\nu = 400 \text{ m}^2 \text{ s}^{-1}$  on the baroclinic deformation radius using alternative values  $R_d = 65$  and  $40 \text{ km}$ . These solutions are qualitatively similar to the standard one with the major differences in the quasi-annual band. When  $R_d = 65 \text{ km}$  the dominant quasi-annual frequency increases by 67%, and with  $R_d = 40 \text{ km}$  it decreases by 47%, suggesting that the frequency is approximately proportional to  $R_d^2$ . This is in agreement with the fact that the characteristic frequency of large-scale Rossby waves is proportional to  $R_d^2$ .

#### b. The 2-layer model

We perform six runs with  $\lambda = 2$  and several values of  $\nu$  (Table 2). The grid resolution is  $15 \text{ km}$  for  $\nu =$



(a)



(b)

FIG. 6. As in Fig. 5 except for the bandpassed solution. Modes (a) and (b) have 29% and 24% of the variance, respectively (CI = 0.02).

$600$  and  $400 \text{ m}^2 \text{ s}^{-1}$ , and  $30 \text{ km}$  for the larger values. Because there is no interfacial friction in the model and because the wind stress acts only on the upper layer, the 2-layer steady states have the lower layer at rest. These steady states are equivalent to the 1.5-layer steady states. However, the stability thresholds are different for the 1.5- and 2-layer gyres; there are previous examples when the 2-layer gyre is less stable (DK, BM2), and it is also true here. We find a stable steady state at  $1500 \text{ m}^2 \text{ s}^{-1}$  and a limit cycle at  $\nu = 1400 \text{ m}^2 \text{ s}^{-1}$ , which suggests the primary Hopf bifurcation occurs at a  $\nu_{cr}$  between these values.

#### 1) NONCHAOTIC ATTRACTORS

The time-mean of the periodic solution at  $1400 \text{ m}^2 \text{ s}^{-1}$  is very similar to Fig. 1a in the upper layer, and in the lower layer it has a weak cyclonic recirculation under the main standing meander and several weaker anticyclonic recirculations near the western boundary. The

TABLE 2. 2-layer model runs with asymmetric ( $\lambda = 2$ ) forcing.

$\nu$	Character	I (%)	Comments (days)
1500	Steady state		
1400	Limit cycle	0.0	PM (195)
1300	Quasiperiodic	50.9	PM (185), SM (630)
1100	Chaotic	18.2	BB ( $\approx 300$ ); low energy events
800	Chaotic	57.4	BB in KE ( $\approx 570$ ); BB in PE ( $\approx 1050$ )
600	Chaotic	67.0	Collection of spikes in KE ( $< 160$ ); PE shows BB at LF
400	Chaotic	77.8	BB (from 200 to 400); interannual peaks; BB at LF

limit cycle period is 195 days, which is smaller than that in the 1.5-layer case (section 2a). Here  $P$  accounts for about 80% of the energy exchange, suggesting a primarily but not purely barotropic instability. This is different from the essentially baroclinic instabilities reported in BM2 and DK. The differences may be due to smaller basins in both of these cases and to the partial-slip boundary condition in DK. The spatial distribution of  $P$  and  $R$  is concentrated near the main standing meander and the southern part of the recirculation. The upper-layer periodic pattern resembles that in the 1.5-layer model. This suggests that both models behave similarly in the vicinity of the primary bifurcation. The lower-layer fluctuations are relatively weak and confined to near the western boundary.

The secondary bifurcation modes have rather different periods in the 1.5- and 2-layer models. The total energy spectrum (Fig. 7a) of quasiperiodic motion at  $\nu = 1300 \text{ m}^2 \text{ s}^{-1}$  demonstrates the secondary bifurcation mode frequency at about  $0.58 \text{ yr}^{-1}$ , or a period of about 630 days. This period is slightly more than two times shorter than in the 1.5-layer model. A period-doubling bifurcation at some critical value for the depth ratio  $\gamma_{cr}$  between zero (the 1.5-layer case) and  $3/37$  (the 2-layer case) may be responsible for this difference (BM2). The dominant frequency of the primary bifurcation mode at  $\nu = 1300 \text{ m}^2 \text{ s}^{-1}$  is  $1.97 \text{ yr}^{-1}$  (period of 185 days), which is slightly larger than that at  $\nu = 1400 \text{ m}^2 \text{ s}^{-1}$ . We filter the quasiperiodic solution around the secondary frequency and find that the pair of leading EOFs contains about 99% of the total variance. The EOF patterns have an upper-layer structure similar to that found in the 1.5-layer solution (Fig. 4). They also have a lower-layer structure of weak westward propagating anomalies in the western part of the basin. The horizontal scale of the anomalies is similar to the scale of the main meander. Barotropic basin modes with the dispersion relationship

$$T = \frac{4\pi^2}{\beta L} (m^2 + n^2)^{1/2}; \quad m = 1, 2, 3 \dots; \\ n = 1, 2, 3 \dots, \quad (11)$$

and linear barotropic unbounded Rossby waves governed by

$$T = \frac{2\pi}{\beta k_x} (k_x^2 + k_y^2) \quad (12)$$

(Pedlosky 1987) are not related to the secondary mode because for periods close to 630 days they either have too short a wavelength and are damped by friction, or they have a wavelength larger than  $L$ .

## 2) BEHAVIOR AT LARGER RE

At higher Re, the dynamics of the 2-layer flow deviates more substantially from the 1.5-layer one. The total energy time series at  $\nu = 1100 \text{ m}^2 \text{ s}^{-1}$  exhibits aperiodic, low-energy events in addition to a statistically stationary background variability. These low-energy events are responsible for some concentration of the power at interannual frequencies (Fig. 7b). The dominant frequency of the background variability is  $\omega = 1.22 \text{ yr}^{-1}$  (period of 300 days). This is 1.5 times smaller than the primary bifurcation mode frequency of the 1.5-layer flow at the same value of  $\nu$ , and its spatial pattern is no longer close to that of primary bifurcation mode, even though the spectrum still exhibits a sharp peak and the viscosity is not much smaller.

In the energy spectrum at  $\nu = 800 \text{ m}^2 \text{ s}^{-1}$  (Fig. 7c), most of the KE is in the mesoscale band, and most of the PE is in the interannual band. This spectral segregation between KE and PE spectra does not occur in the 1.5-layer model and in the early bifurcations of the 2-layer circulation. The EOF analysis of the solution filtered around the spectrum peak at  $\omega = 0.38 \text{ yr}^{-1}$  shows a spatial pattern concentrated around the main meander. In the solutions at  $\nu = 600$  and  $400 \text{ m}^2 \text{ s}^{-1}$  (Fig. 7d), most of the KE still belongs to the quasi-annual and mesoscale bands, although it progressively leaks to the interannual band with increasing Re. The PE concentration in the interannual band continues to increase with Re. The total energy partition at  $\nu = 400 \text{ m}^2 \text{ s}^{-1}$  is  $I = 80.5\%$ ,  $Q = 17.2\%$ , and  $M = 2.3\%$ . The low-order moments (10) of the energy time series are  $D = 0.042$  (slightly smaller than in the 1.5-layer case),  $S = -0.25$  (indicating more distinctive low-energy events), and  $K = 2.90$  (indicating substantial intermittency).

Compared with the 1.5-layer model, the time-mean circulation at  $\nu = 400 \text{ m}^2 \text{ s}^{-1}$  (Fig. 8) shows the separation point of the eastward jet retreating southward to approximately the middle of the basin, with the eastward jet becoming more intense and narrow and penetrating farther to the east. The time-mean lower layer flow

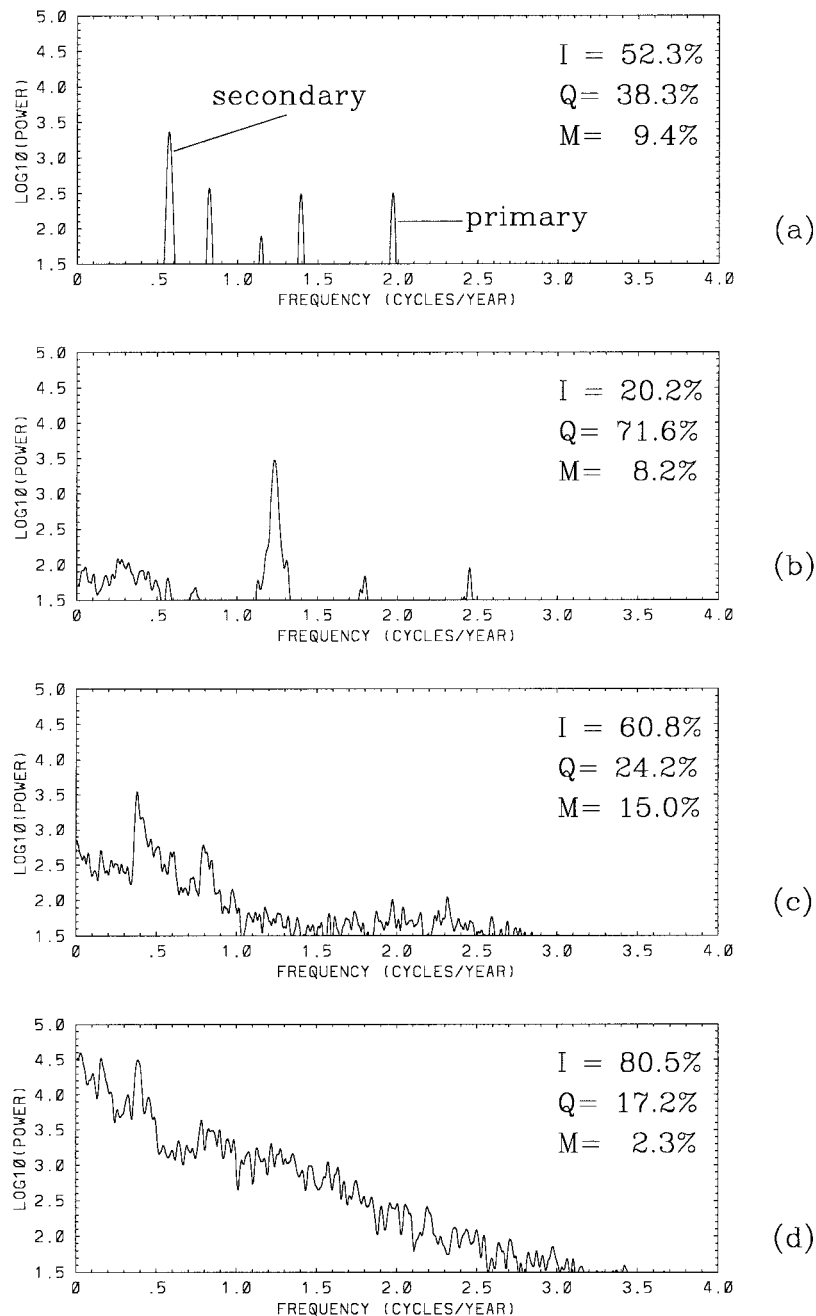


FIG. 7. Energy spectra for 2-layer solutions with  $\lambda = 2$ : (a)  $\nu = 1300 \text{ m}^2 \text{ s}^{-1}$ , (b)  $\nu = 1100 \text{ m}^2 \text{ s}^{-1}$ , (c)  $\nu = 800 \text{ m}^2 \text{ s}^{-1}$ , and (d)  $\nu = 400 \text{ m}^2 \text{ s}^{-1}$ . In the legends I, Q, and M denote the relative power in the interannual, quasi-annual, and mesoscale frequency bands, respectively.

shows a standing vortex street, as in Verron and Le Provost (1991). The instantaneous patterns of the flow show strong meandering of the eastward jet and subsequent shedding of rings, as well as generation of baroclinic eddies in the return flow (Holland 1978). The southward retreat of the separation point suggests that the generation of potential vorticity by the wind is balanced to a lesser extent by the potential vorticity flux

from the western boundary and to a greater extent by fluid exchange across the eastward jet. The energy diagram of the circulation (Fig. 9) shows that more energy goes to fluctuations rather than dissipates by the time-mean field. It also shows that the barotropic  $P$  and baroclinic  $R$  conversion rates (appendix B) have approximately equal values integrated over the basin.

We lowpass (i.e., for  $\omega < 0.58 \text{ yr}^{-1}$ ) filter the solution

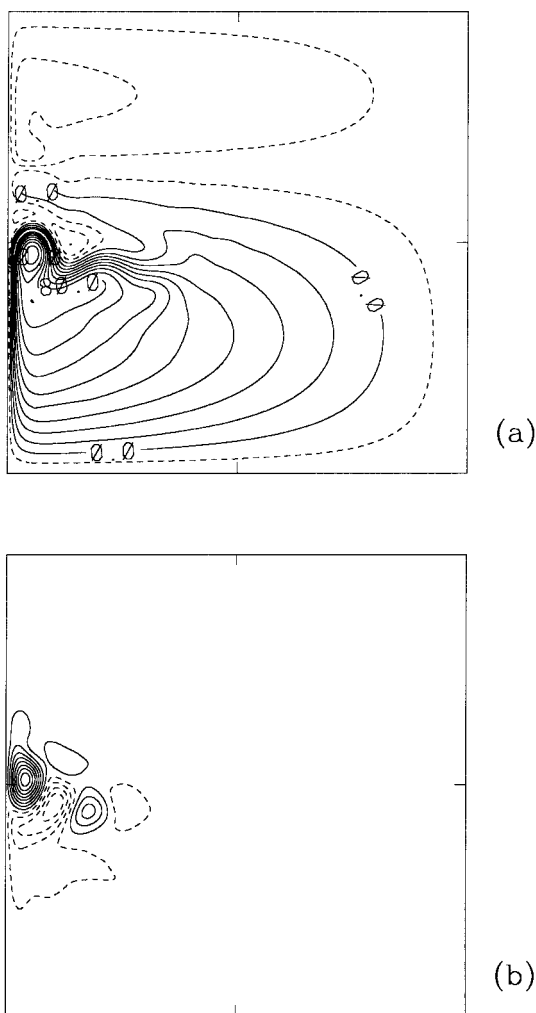


FIG. 8. The 2-layer, time-mean circulation with  $\lambda = 2$  and  $\nu = 400 \text{ m}^2 \text{ s}^{-1}$ : (a)  $\langle \psi_1 \rangle$  ( $\text{CI} = 10 \times 10^3$ ), (b)  $\langle \psi_2 \rangle$  ( $\text{CI} = 10^3$ ).

with  $\nu = 400 \text{ m}^2 \text{ s}^{-1}$  and perform an EOF analysis. The EOFs show that the most substantial variability occurs around the eastward jet, with weaker variability near the western boundary. The leading pair of EOFs (Fig. 10) contains 29% of the variance in the first mode and 19% in the second. Both EOFs have anomalies in the upper layer aligned parallel to the eastward jet. The first function corresponds to north–south shifting of the jet from its mean position. The second function represents strengthening and weakening of the jet and the associated countercurrents to the north and south of it: when the jet accelerates, the countercurrents become stronger. From the time series of the first and second EOF amplitudes (Fig. 11), we find that the first EOF leads by about 600 days, with a maximum time-lag correlation of 0.3.

We highpass ( $\omega > 0.58 \text{ yr}^{-1}$ ) filter the same solution in order to compare the combined quasi-annual and mesoscale variability with the interannual variability. The

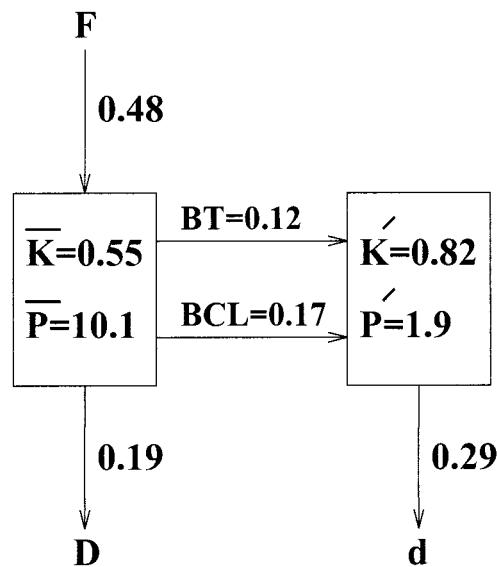


FIG. 9. Energy diagram for the 2-layer solution with  $\lambda = 2$  and  $\nu = 400 \text{ m}^2 \text{ s}^{-1}$ .

leading EOFs of the highpass fields (Fig. 12) are qualitatively similar to the quasi-annual 1.5-layer model EOFs (Fig. 6), although the associated horizontal scale is smaller here. The overall variability pattern seems to be related to local mesoscale instabilities of the eastward jet, rather than to the global changes associated with amplifications and shifts of the jet axis. The maximum time-lag correlations between pairs of the four leading EOFs range from 0.2 to 0.4, suggesting appreciable dynamical coupling among all of them.

How are the dynamics different during different phases of the low-frequency variability? We now examine four states corresponding to maxima and minima for each of the first and second lowpass EOFs. The system is defined to be in a high (low) state when the corresponding EOF amplitude is larger (smaller) than the mean-squared deviation of its time series. Conditional averages and corresponding energy balances are calculated for each of these states. When the eastward jet is shifted northward, the first EOF amplitude is positive. When the eastward jet is shifted southward, the first EOF amplitude is negative. The northern (Fig. 13a) and southern (Fig. 13b) states have qualitatively similar energy balances, characterized by moderate conversion rates with a dominant baroclinic conversion. In contrast, fluctuations associated with the second EOF change the energy balances quite substantially. When the eastward jet is short (i.e., the second EOF has large positive values), the energy conversions (Fig. 13c) are the largest, and the barotropic conversion BT dominates the baroclinic conversion BCL. In this state, the mean circulation is the weakest, and perturbations are the most energetic. When the eastward jet is long, the energy conversion magnitude is moderate with a strong dominance by the baroclinic conversion. In this state, the mean

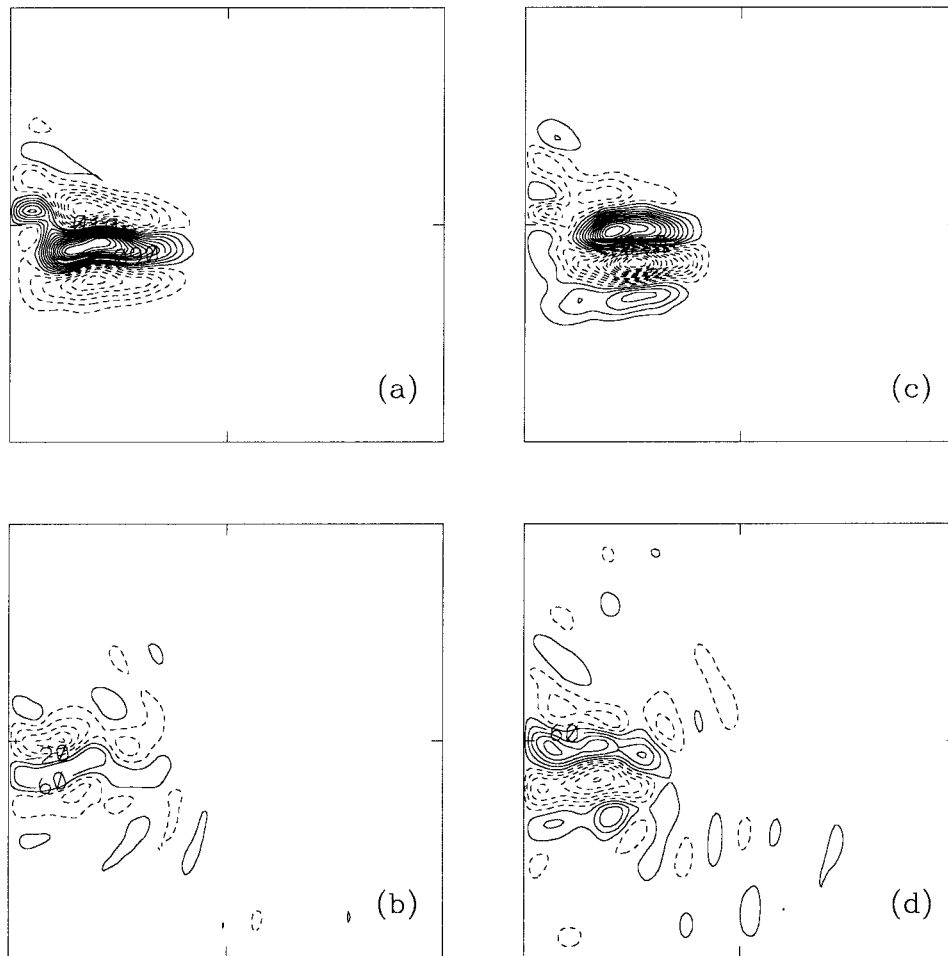


FIG. 10. EOF representation of the low-passed 2-layer solution with  $\lambda = 2$  and  $\nu = 400 \text{ m}^2 \text{ s}^{-1}$ . The first and second EOFs have 29% and 19% of the total variance, respectively. (a) and (b) EOF1 in upper and lower layers [(a) CI = 0.02; (b) CI = 0.004]; (c) and (d) EOF2 in upper and lower layers [(c) CI = 0.02; (d) CI = 0.004].

circulation is the strongest, and perturbations are the least energetic.

The total energy conversion density due to the contribution by baroclinic conversion  $R$  (not shown) has negative values along the eastward extension of the eastward jet, suggesting that the jet is maintained, both in the full time-mean and in the low-frequency variability states, by the isopycnal form stresses associated with shed eddies with a locally negative eddy-diffusivity behavior (i.e., the vector dot product of the horizontal eddy buoyancy flux with the mean horizontal buoyancy gradient is positive).<sup>1</sup> This relation between the eddies and

the mean flow in the offshore end of the eastward jet (i.e., negative  $R$ ) is contrary to the famous example of negative eddy-viscosity behavior associated with the horizontal Reynolds stresses in the core of a broad, baroclinically unstable eastward jet, like the atmospheric jet stream (Holton 1992) and the Antarctic Circumpolar Current (McWilliams and Chow 1981), where  $R$  is positive and  $P$  is negative. However, we checked that the primary contribution to  $R < 0$  in this region arises from the rotational component of the eddy buoyancy flux

$$\langle [-\mathbf{x}(\psi'_{1y} + \psi'_{2y}) + \mathbf{y}(\psi'_{1x} + \psi'_{2x})](\psi'_1 - \psi'_2) \rangle,$$

rather than from the divergent component (e.g., Marshall and Shutts 1981). Therefore, it is perhaps more appropriate to interpret  $R$  here as the divergence of a baroclinic eddy transport of mean energy—a spatial rearrangement—rather than as a locally negative eddy diffusivity of mean buoyancy—a reverse generation of eddy energy.

<sup>1</sup> We believe that this is a robust behavior for the offshore extension of the eastward jet in ocean gyres. An example of similar behavior can be seen in the left-hand panels of Fig. 12 in McWilliams et al. (1990), for a different set of gyre solutions, although it is obscured by a previously unnoticed—hence undeclared—sign error in these two panels.

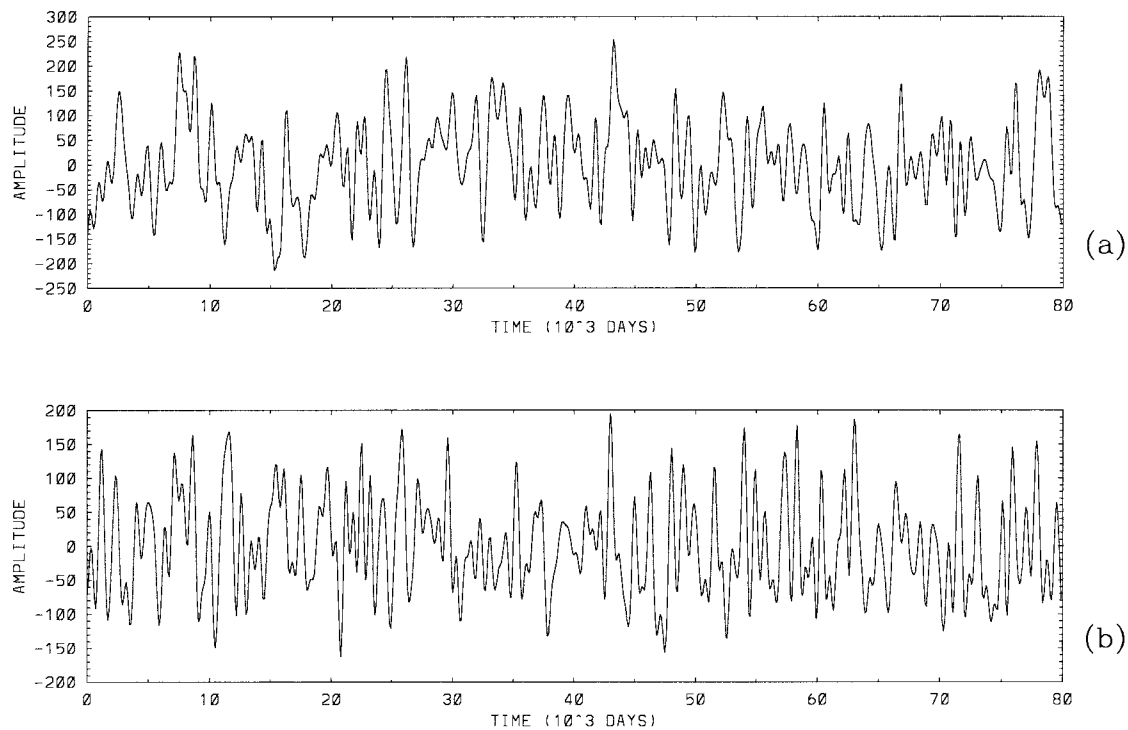


FIG. 11. EOF time series for the the modes in Fig. 10.

Fixing  $\nu = 400 \text{ m}^2 \text{ s}^{-1}$ , we explore  $R_d = 65$  and  $40$  km. In the former case, the flow behavior shows no significant qualitative changes in comparison with  $R_d = 52$  km, except the spectral power shifts toward higher frequencies ( $I = 53.0\%$ ,  $Q = 35.2\%$ , and  $M = 11.8\%$ ); this shift is similar to that in the 1.5-layer model. With  $R_d = 40$  we find some qualitative changes in the flow associated with the local instability in the western boundary current of the subtropical gyre. The instability bursts irregularly on the interannual timescale and results in an intense meandering of the western boundary current, a subsequent weakening of the eastward jet, and a substantial decrease of the flow energy. The global influences of local western boundary current instability are a subject of another paper (Berloff and McWilliams 1999).

### 3. Symmetric forcing

#### a. The 1.5-layer model

The symmetric ( $\lambda = 0$ ) 1.5-layer problem has been more extensively investigated than the others we discuss in this paper. Here we calculate the seven solutions summarized in Table 3. The grid resolution is  $15$  km. A symmetric steady state is found at  $\nu = 1400 \text{ m}^2 \text{ s}^{-1}$ , and a pair of nonsymmetric steady states is found at  $\nu = 1200 \text{ m}^2 \text{ s}^{-1}$ ; the latter arise by a pitchfork bifurcation (Cessi and Ierley 1995; Speich et al. 1995) at some intermediate  $\nu_{\text{cr}}$ .

#### 1) NONCHAOTIC ATTRACTORS

Each nonsymmetric steady state has recirculations trapped near the western boundary and separated by the eastward jet, and each state loses stability via Hopf bifurcation at another  $\nu_{\text{cr}}$  somewhat lower than  $1200 \text{ m}^2 \text{ s}^{-1}$ . We find a periodic solution corresponding to the northern state (the eastward jet is shifted to the north) at  $\nu = 1100 \text{ m}^2 \text{ s}^{-1}$ . It has a period of 236 days and a small amplitude (0.2% of the total energy). The periodic solution is similar to the most unstable eigenmode of the associated steady state that is centered around the jet and recirculations but also has a propagating Rossby wave pattern in the basin interior (Jiang et al. 1995).

At  $\nu = 1000 \text{ m}^2 \text{ s}^{-1}$  the circulation corresponds to phase-locked (PL) motion on a torus, due to a secondary Hopf bifurcation at some  $\nu_{\text{cr}}$  between  $1000$  and  $1100 \text{ m}^2 \text{ s}^{-1}$  (e.g., BM1). The phase-locking frequency ratio is  $1/8$ , so the secondary mode has a dominant frequency of  $\omega = 0.197 \text{ yr}^{-1}$  (period of 1850 days). The total energy spectrum (Fig. 14) has a comblike shape due to nonlinear interactions involving the primary and secondary modes (frequency differences between the neighboring peaks are equal to the secondary mode frequency), and it shows that most of the power (due to the PE contribution) is concentrated in the secondary mode. The difference in power between the primary and secondary modes is not observed in the asymmetric solutions above. We filter the PL solution around the secondary frequency and decompose it in the pair of EOFs

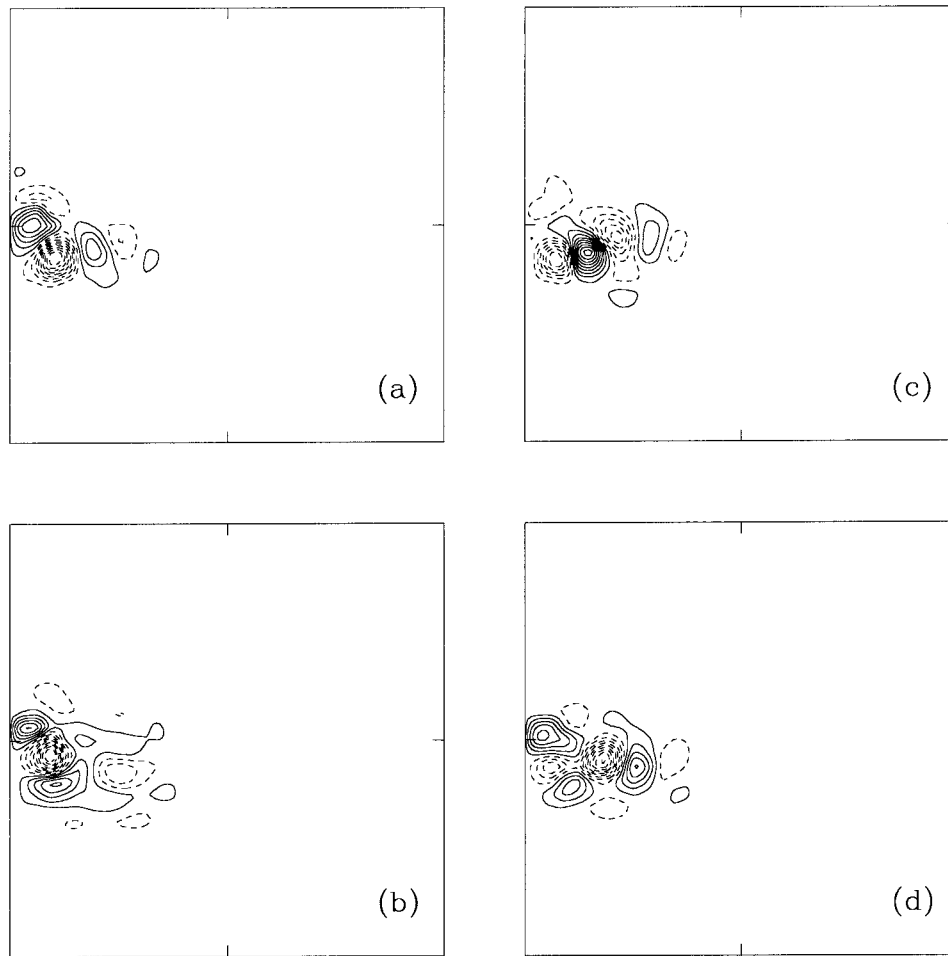


FIG. 12. The upper-layer patterns of the four leading EOFs [in (a)–(d)] for the high-passed, 2-layer solution with  $\lambda = 2$  and  $\nu = 400 \text{ m}^2 \text{ s}^{-1}$ . The fractional variances are 24%, 18%, 13%, and 10%, respectively (CI = 0.05).

(Fig. 15). The EOFs have anomalies at the recirculation zone and decay away from it. In comparison with the asymmetric secondary bifurcation mode (Fig. 4), the EOFs correspond to a relatively large-scale spatial pattern that is consistent with the dominance of PE in the secondary bifurcation mode.

## 2) BEHAVIOR AT LARGER RE

The circulations are qualitatively similar at  $\nu = 800$  and  $700 \text{ m}^2 \text{ s}^{-1}$ . The energy time series at  $\nu = 700 \text{ m}^2 \text{ s}^{-1}$  (Fig. 16a) has its maximum spectral power at  $0.215 \text{ yr}^{-1}$  (period of 1700 days). The spectral maximum can plausibly be traced to the secondary bifurcation mode at lower Re. The primary mode has some remnants in the spectra as a weak and broad intermonthly band around  $\omega = 2.03 \text{ yr}^{-1}$ . Thus, the temporal behavior is primarily interannual with small intermonthly fluctuations.

The circulation changes substantially when  $\nu$  is re-

duced to  $600 \text{ m}^2 \text{ s}^{-1}$ . The recirculation zones (or the recirculating dipole) become very intense and diverge from the wall-trapped state at lower Re. The energy time series (Fig. 16b) shows very strong and aperiodic oscillations with most of the spectral power contained in interannual and longer timescales (e.g., McCalpin and Haidvogel 1997). The time series from Fig. 16b has its greatest spectral power at about 30 yr. Due to the finite solution integration length (400 yr), we are uncertain whether the spectrum has its maximum power at a small but finite frequency, or whether rare strong events push the maximum to smaller frequencies over longer intervals.

In spite of the strong aperiodicity the spatial structure of the flow during one temporal cycle is robust. The sequence of instantaneous  $\psi_1$  fields during a cycle is shown in Fig. 17. The high energy state of the flow (panel 1) contains a very intense recirculation dipole in one of the two nonsymmetric states identical through the mirror symmetry transformation:  $y \rightarrow -y$ ,  $\psi_1 \rightarrow$

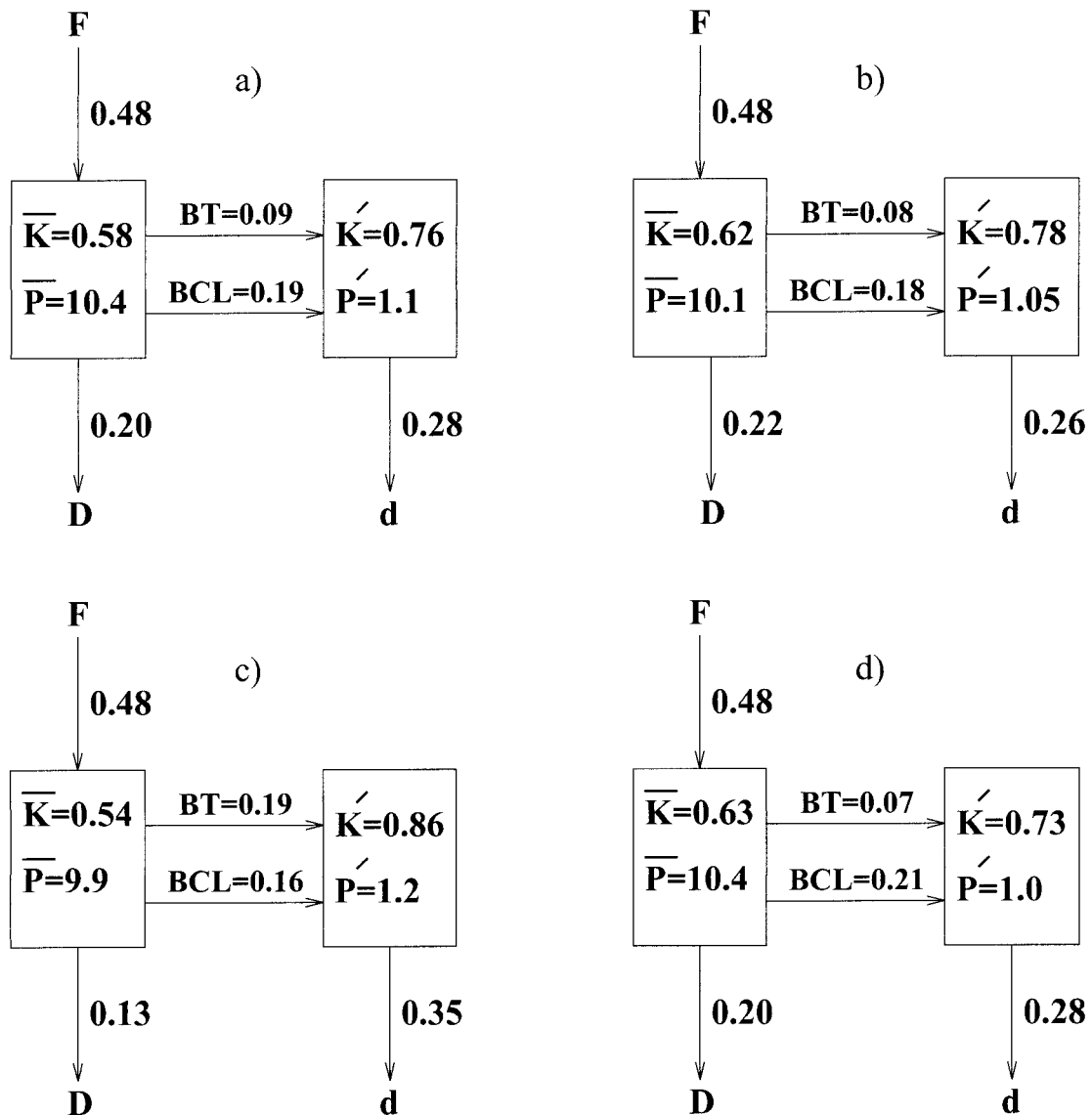


FIG. 13. Energy diagrams for the 2-layer solution with  $\lambda = 2$  and  $\nu = 400 \text{ m}^2 \text{ s}^{-1}$ , based on conditional averages when the eastward jet is shifted to the north (a) or south (b), or when the eastward jet is relatively short (c) or long (d).

$-\psi_1$ . This state persists for an uncertain period from a few years to a decade or so. During this time the degree of asymmetry in the dipole grows very slowly (panel 2). Then, during a few more years, the system experiences a dramatic change (panels 3–5) associated with

the complete destruction of the dipole and the appearance of several eddies in its place. After that, the circulation reaches its energy minimum, and a new dipole begins to develop (panel 6). The dipole grows into either one of the two nonsymmetric states and the cycle re-

TABLE 3. 1.5-layer model runs with asymmetric ( $\lambda = 2$ ) forcing.

$\nu$	Character	I (%)	Comments (days)
1400	Steady state		Symmetric
1200	Steady state		Nonsymmetric
1100	Limit cycle	0.0	PM (236), small amplitude
1000	Phase locking	99.4	Ratio: $\frac{1}{2}$ , SM (1850)
800	Chaotic	98.5	BB ( $\approx 2100$ )
700	Chaotic	98.5	BB ( $\approx 2100$ )
600	Chaotic	99.9	Very strong and aperiodic interdecadal oscillations

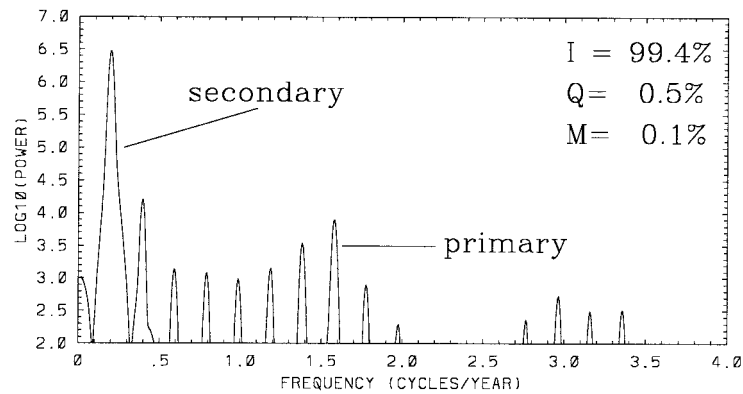


FIG. 14. Energy spectrum for 1.5-layer solution with  $\lambda = 0$  and  $\nu = 1000 \text{ m}^2 \text{ s}^{-1}$ .

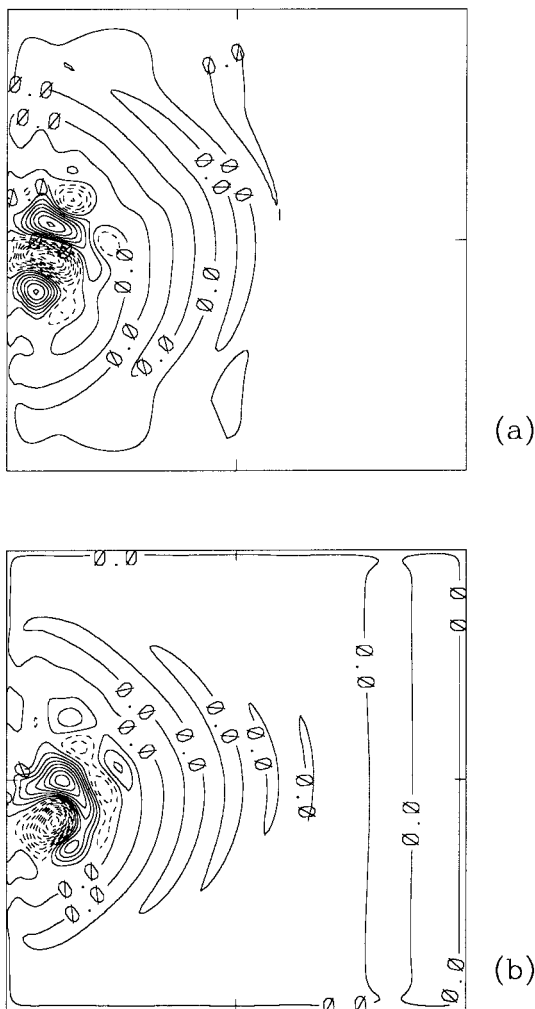


FIG. 15. EOF representation of the secondary bifurcation mode of the 1.5-layer solution with  $\lambda = 0$  and  $\nu = 1000 \text{ m}^2 \text{ s}^{-1}$  (CI = 0.02).

peats. The switching between the states can be illustrated by following the flow separation points at the western boundary (Fig. 18). The separation point is associated with the vorticity changing sign at the wall (located by linear interpolation). Transitions between the nonsymmetric states occur on an interdecadal timescale.

How relevant are the primary and secondary bifurcation modes at large  $\text{Re}$ ? It is possible that the secondary bifurcation mode transforms into the aperiodic wall-trapped oscillations at  $\nu = 700 \text{ m}^2 \text{ s}^{-1}$  and then further into the stronger and slower oscillations at  $\nu = 600 \text{ m}^2 \text{ s}^{-1}$ . Aspects of the behavior of the primary bifurcation are still present at  $\nu = 600 \text{ m}^2 \text{ s}^{-1}$  in the form of weak noise (Fig. 16b), but this is dwarfed by the dominant cycle of the dipole growth and destruction.

What is the physical mechanism governing the dipole cycle? One possibility is that the dynamics is controlled by the underlying unstable steady states of the flow (Primeau 1998), that is, by the equilibrium (fixed) points of the associated large-dimensional dynamical system. In this case, the motion occurs on a chaotic attractor in the vicinity of an orbit homoclinic<sup>2</sup> (e.g., Drazin 1992) to a fixed saddle point. The system approaches the fixed point along the stable manifold (this would correspond to the gradual amplification of the dipole), slows down in the vicinity of the fixed point, and runs away along the unstable manifold (e.g., Drazin 1992). We have not yet calculated the unstable steady states here to test this hypothesis.

What happens at higher  $\text{Re}$ ? This is probably not relevant for the following reason. The flow velocity in the first panel of Fig. 17 reaches very large values of  $0.7 \text{ m s}^{-1}$  in the western boundary currents and  $1.3 \text{ m s}^{-1}$  in the eastward jet. In a model permitting baroclinic instability, such a flow would become unstable, and the gyre dynamics would be substantially modified (see section 3b). Nevertheless, for uniformity with other con-

<sup>2</sup> A *homoclinic orbit* is an orbit connecting a saddle equilibrium point with itself, approaching the point as  $t \rightarrow \pm\infty$ . A homoclinic orbit corresponds to a solution of infinite "period."

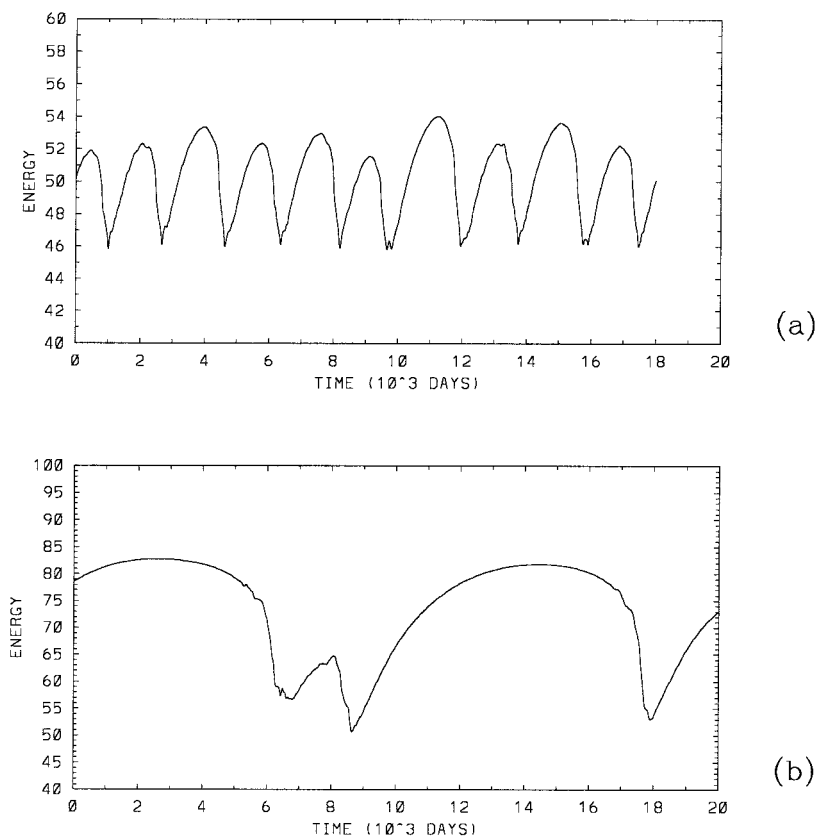


FIG. 16. Energy time series for 1.5-layer solution with  $\lambda = 0$ : (a)  $\nu = 700 \text{ m}^2 \text{ s}^{-1}$  and (b)  $\nu = 600 \text{ m}^2 \text{ s}^{-1}$ .

figurations, we run the model with  $\nu = 400 \text{ m}^2 \text{ s}^{-1}$  (7.5-km grid resolution) and find that the flow exhibits even more unrealistically strong oscillations with an energy fluctuation two times stronger than in Fig. 16b. The low-order moments (10) of the energy time series yield a very non-Gaussian distribution with several distinct preferred states similar to what is shown in McCalpin and Haidvogel (1997). The relative deviation  $D = 0.277$  is the largest found in our study.

Fixing  $\nu = 600 \text{ m}^2 \text{ s}^{-1}$ , we explore  $R_d = 40$  and 65 km. For  $R_d = 40$  km, the timescale of the dominant cycle increases by about twice, perhaps because the circulation stays closer to the underlying unstable steady state. In contrast, no substantial changes are found with  $R_d = 65$  km. All this suggests that in the symmetric case the timescale of the dominant cycle has a different dependence on  $R_d$  than that of large-scale Rossby waves or local instability of the western boundary current.

### b. The 2-layer model

#### 1) NONCHAOTIC ATTRACTORS

We calculate the five solutions with  $\lambda = 0$  listed in Table 4. The grid resolution is 15 km. We find a non-symmetric steady state (coinciding with the 1.5-layer

steady state) at  $\nu = 1200 \text{ m}^2 \text{ s}^{-1}$ . The flow experiences two successive Hopf bifurcations at some  $\nu_{cr}$  between 1200 and  $1000 \text{ m}^2 \text{ s}^{-1}$ , and there is quasiperiodic motion at  $\nu = 1000 \text{ m}^2 \text{ s}^{-1}$ . The dominant frequencies and the upper-layer spatial patterns of the primary and secondary bifurcation modes are similar to those of the 1.5-layer model, and the lower-layer disturbances are relatively weak.

#### 2) BEHAVIOR AT LARGER RE

The behavior for  $\nu = 800 \text{ m}^2 \text{ s}^{-1}$  is chaotic, but otherwise the deviations from the 1.5-layer model are still modest. However, at  $\nu = 600 \text{ m}^2 \text{ s}^{-1}$ , the 2-layer energy time series (Fig. 19a) differs from the corresponding 1.5-layer series (Fig. 16b) in several ways. In the 2-layer case the amplitudes of different cycles have similar values, the deviations from the time-mean are much smaller, and the dominant timescale is much shorter (about 7 yr). Here the cycle comprises three distinct states. In the first state (Fig. 20a), the flow energy is at minimum, and there are one or two relatively weak eastward jets with several eddies around them. The transition between the first and second states takes about 2–5 yr, and when the second state is reached (Fig. 20b) the energy is at

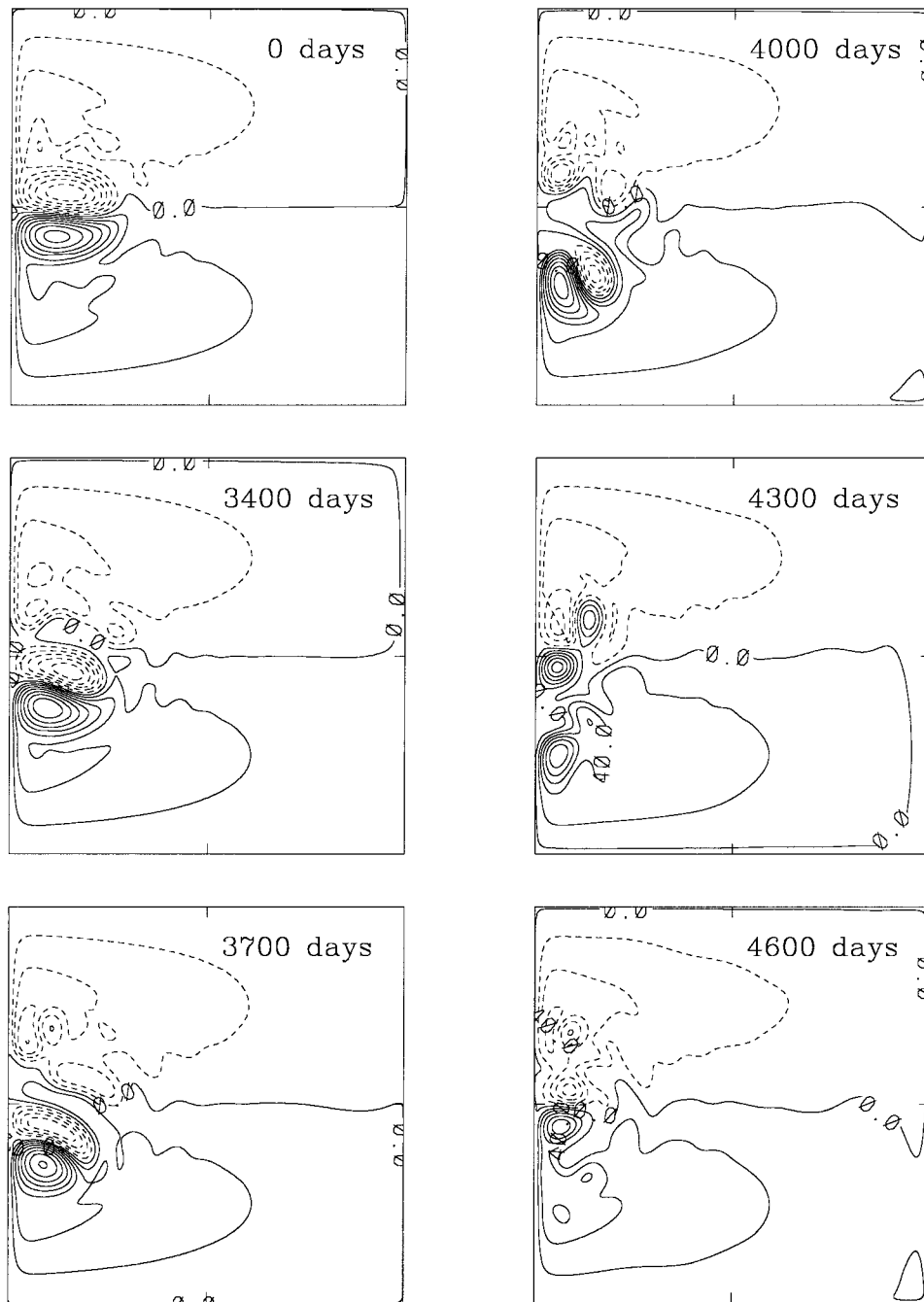


FIG. 17. Instantaneous  $\psi_1$  fields during the dominant cycle in the 1.5-layer solution with  $\lambda = 0$  and  $\nu = 600 \text{ m}^2 \text{ s}^{-1}$  ( $\text{CI} = 20 \times 10^3$ ).

maximum. In this state the recirculations in the upper layer are well developed, but the lower-layer flow is weak. During the transition between the second and third states (1–2 yr), the northern and southern flanks of the recirculations become baroclinically unstable and the large-scale circulation loses energy. This behavior is consistent with the fact that westward currents on the  $\beta$  plane are, in general, less stable than the eastward

ones (Pedlosky 1987). The third, metastable state (Fig. 20c) contains mesoscale eddies generated on both flanks of the recirculation zones. The temporal variability associated with the vortices appears as the high-frequency noise (see Fig. 19a) imposed on the dominant oscillations. During the transition back to the first state (2–3 yr), the dipole collapses into several eddies. We find that transitions from one mirror image to another are

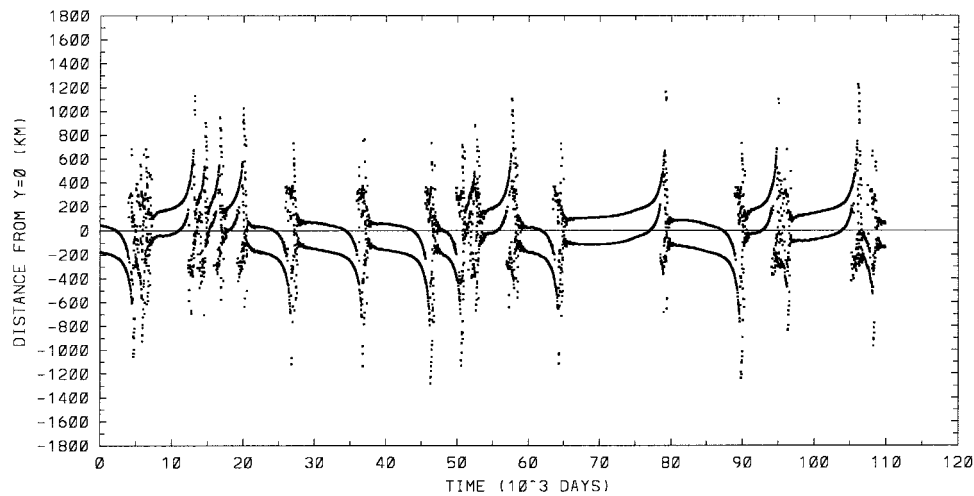


FIG. 18. Locations of the meridional separation point on the western boundary for the 1.5-layer solution with  $\lambda = 0$  and  $\nu = 600 \text{ m}^2 \text{ s}^{-1}$ .

very rare in the 2-layer situation (we see only a single transition in a 300-yr integration).

When  $\nu$  is reduced to  $400 \text{ m}^2 \text{ s}^{-1}$ , the jet penetrates to the middle of the basin and meanders weakly. There are about 4–5 westward propagating eddies in each recirculation zone. The propagation periods are slightly different for the streets and both are about 120 days. A time-average of the state with the jet shifted to the south (Fig. 21) contains a meridional sequence of four zonally elongated recirculation cells in the lower layer (Verron et al. 1987). The sequence is different from the deep vortex street with  $\lambda = 2$  (Fig. 8). The total energy time series (Fig. 19b) shows infrequent events with particularly low energy. The energy minima correspond to particularly strong destructions of the eastward jet (Fig. 20a) that may last for several years. During such events the separated western boundary currents split into two distinct eastward jets (as in the no-slip solutions in Haidvogel et al. 1992).

The energy time series has the low-order moments:  $D = 0.046$ , a particularly negative  $S = -1.17$  associated with the increased probability of the anomalously low energy events, and a relatively large  $K = 2.08$ . A low-pass ( $\omega < 0.58 \text{ yr}^{-1}$ ) EOF analysis has its first two modes with 60% and 17% of the total variance. The first EOF is symmetric with respect to the middle of the basin (implying a north–south shift of the jet axis) and

the second one is antisymmetric. In this regard they are qualitatively similar to the leading, low-pass EOF pair with  $\lambda = 2$  (Fig. 10); however, the  $\lambda = 0$  solution has a behavior with distinctive regime transitions, rather than more continuous variations. Thus, its first EOF is relatively more dominant. The largest time-lag correlation between the EOFs here is rather small (about 0.1) because the regime transitions occur very irregularly.

As in section 2b we calculate conditional energy balances in situations when the jet is in the northern (amplitude of the first EOF has positive values larger than the mean-squared deviation from zero) or southern (negative values) states (Fig. 22a). These two states are energetically equivalent because of the meridional symmetry of the wind. The barotropic conversion BT dominates; the ratio of the perturbation to the mean-flow energy is about half that with  $\lambda = 2$ ; and the energy dissipates mainly through the mean flow. When the jet is in either “short” (shown as a split-jet pattern in Fig. 22b) or “long” states (Fig. 22c), the baroclinic conversion is close to zero, the mean circulation is weaker, and the perturbations are stronger than the states with meridional shifts in the jet position. Comparing the two states, the ratio of mean to eddy energies is larger for the long jet (as with  $\lambda = 2$ ); however, we do not see a strong baroclinic conversion dominance here for the long jet (unlike with  $\lambda = 2$ ). The eastward end of the

TABLE 4. 2-layer model runs with asymmetric ( $\lambda = 2$ ) forcing.

$\nu$	Character	I (%)	Comments (days)
1200	Steady state		Nonsymmetric
1000	Quasiperiodic	100.0	PM (240), SM (5 years)
800	Chaotic	99.1	Wall-trapped dipole oscillations ( $\approx 3100$ )
600	Chaotic	98.4	Runaway dipole oscillations (the timescale is twice shorter than with 1.5 layers)
400	Chaotic	98.5	BB ( $\approx 6300$ ); (LF growth is due to rare low-energy events)

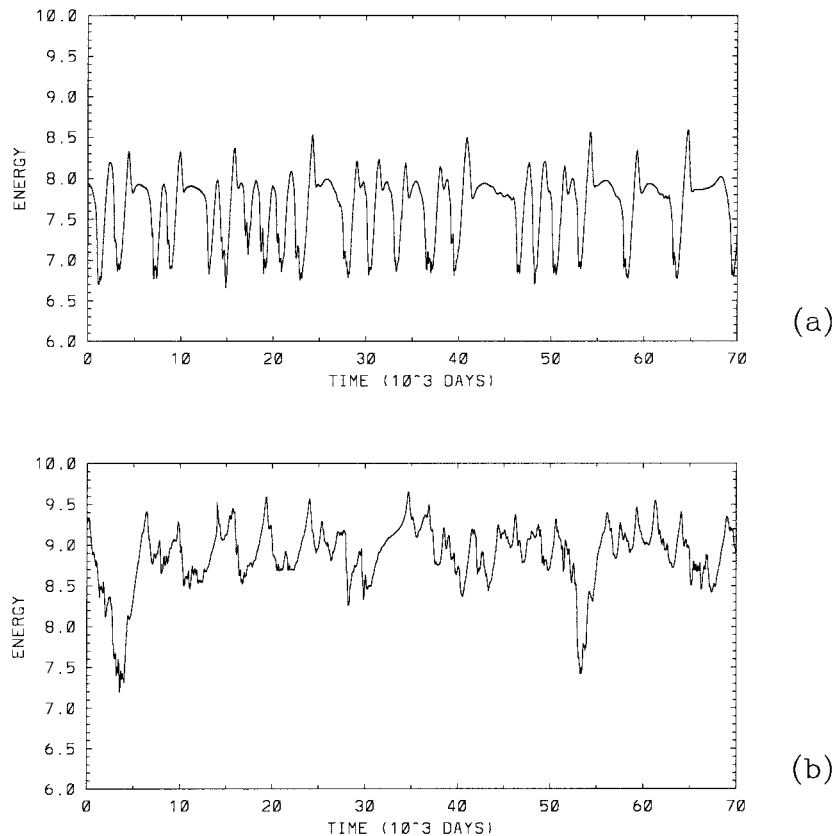


FIG. 19. Energy time series for 2-layer solution with  $\lambda = 0$ : (a)  $\nu = 600 \text{ m}^2 \text{ s}^{-1}$  and (b)  $\nu = 400 \text{ m}^2 \text{ s}^{-1}$ .

eastward jet is again a region of negative energy conversion (i.e., negative eddy-diffusivity behavior) due to the contribution from the baroclinic energy conversion  $R(x, y)$ .

The flow with  $\nu = 400 \text{ m}^2 \text{ s}^{-1}$  is substantially stabilized when  $R_d$  equals 65 km due to suppressed baroclinic instability in the recirculation zones. Its energy fluctuates by less than 3%, the flow is quasiperiodic (with periods of 104 and 3500 days), the eastward jet is persistent, and the flow in the lower layer is weaker. With  $R_d = 40 \text{ km}$ , the eastward jet fluctuates between the two preferred states, one of which corresponds to the low-energy state and a long eastward jet and the other to the high-energy state and a short jet. The time-scale of the fluctuations is about 3500 days. The main difference from  $R_d = 52 \text{ km}$  is that the jet is never completely destroyed.

#### 4. Discussion and conclusions

The spatiotemporal variability of midlatitude oceanic gyres driven by a steady wind is investigated in 1.5- and 2-layer QG models as a function of  $Re$ . We address and partially answer the fundamental questions posed in section 1a.

Two types of wind forcing are considered: one sym-

metric with respect to middle latitude and one asymmetric. In each situation two early bifurcations and their corresponding flow patterns are identified. Also, several solutions are analyzed with  $Re$  relatively far from  $Re_{cr}$  corresponding to the first Hopf bifurcation. The large-scale, low-frequency variability is analyzed by the energy time series, the circulation patterns, and EOF decompositions of the complete and filtered solution fields.

The hierarchy of idealized wind-driven circulation models studied shows that the more generic LF variability arises when the wind forcing is strongly asymmetric, the Reynolds number  $Re$  is relatively large, and the baroclinic instability mechanism is active in the flow.

The primary and secondary bifurcation modes are rather similar in both the 1.5- and 2-layer models. The primary mode corresponds to intermonthly variability. It is characterized by the presence of Rossby waves in the interior and by the mesoscale instability in the western part of the basin. The secondary mode has an interannual timescale and is more confined to the western part of the basin. As  $Re$  is further increased beyond the bifurcation values, several general tendencies are seen: the spectrum bandwidth increases, the fraction of the power at low frequency increases, and the associated spatial pattern has a large spatial scale.

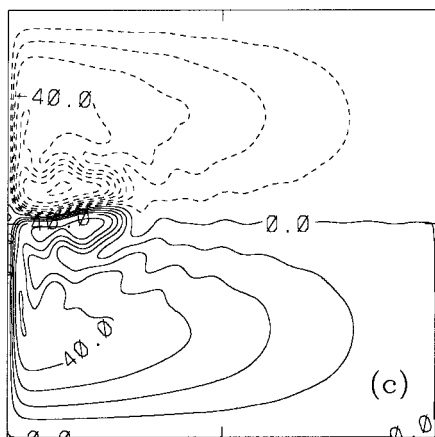
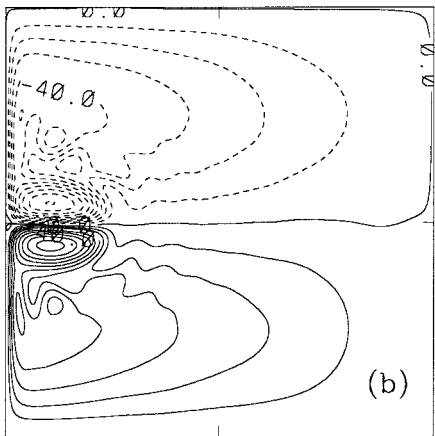
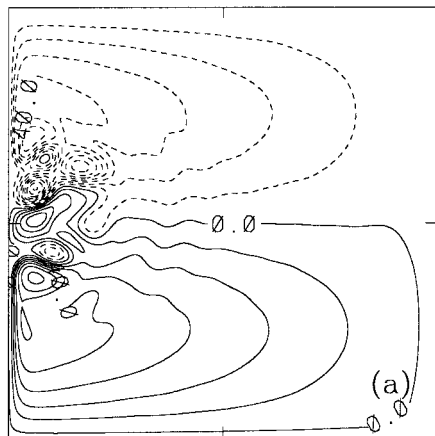


FIG. 20. Instantaneous  $\psi_1(x, y)$  in the 2-layer solution with  $\lambda = 0$  and  $\nu = 600 \text{ m}^2 \text{ s}^{-1}$  during (a) low-energy, (b) high-energy, and (c) metastable states ( $\text{CI} = 10 \times 10^3$ ).

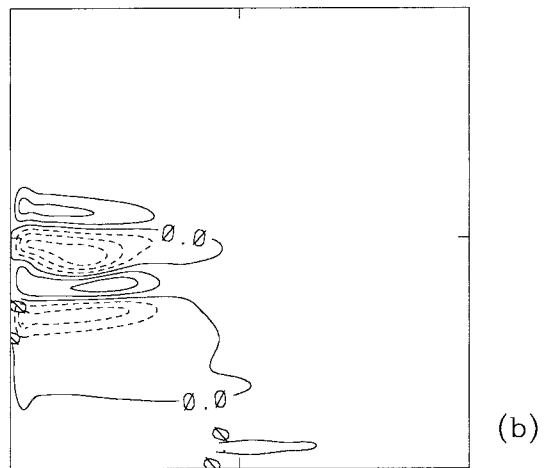
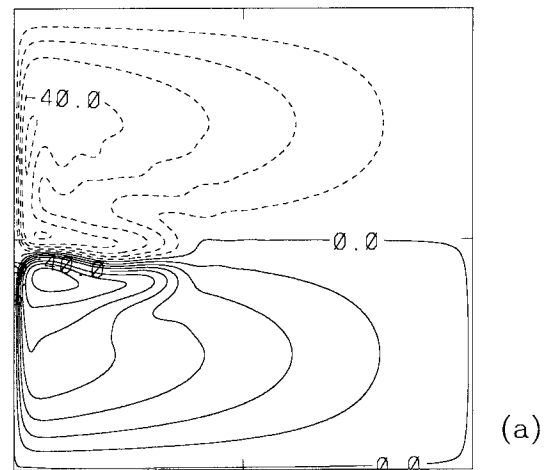


FIG. 21. Time-mean circulation in the 2-layer solution with  $\lambda = 0$  and  $\nu = 400 \text{ m}^2 \text{ s}^{-1}$ : (a)  $\psi_1(x, y)$  ( $\text{CI} = 10 \times 10^3$ ) and (b)  $\psi_2(x, y)$  ( $\text{CI} = 0.5 \times 10^3$ ).

At high  $\text{Re}$  the asymmetrically forced 1.5-layer model has most of its spectral power in two well-separated frequency bands. One band corresponds to quasi-annual ( $0.9 \div 1.3 \text{ yr}$ ) periods that increase with increasing  $\text{Re}$ . The spatiotemporal variability patterns within this band have dominant perturbations around the separated eastward current and Rossby wavelike disturbances in the interior of the basin; thus, they have characteristics qualitatively similar to the primary bifurcation mode but differ in the details of the pattern. The other dominant frequency band is for periods longer than 3.5 yr. Its primary patterns have a larger spatial scale than in the quasi-annual band. They correspond to either intensification or meridional displacement of the separated eastward current and its recirculation zones with time-lag correlations between the patterns that imply a cyclonic rotation of anomalies. The 2-layer solution differs in several ways from the 1.5-layer one at high  $\text{Re}$ . The

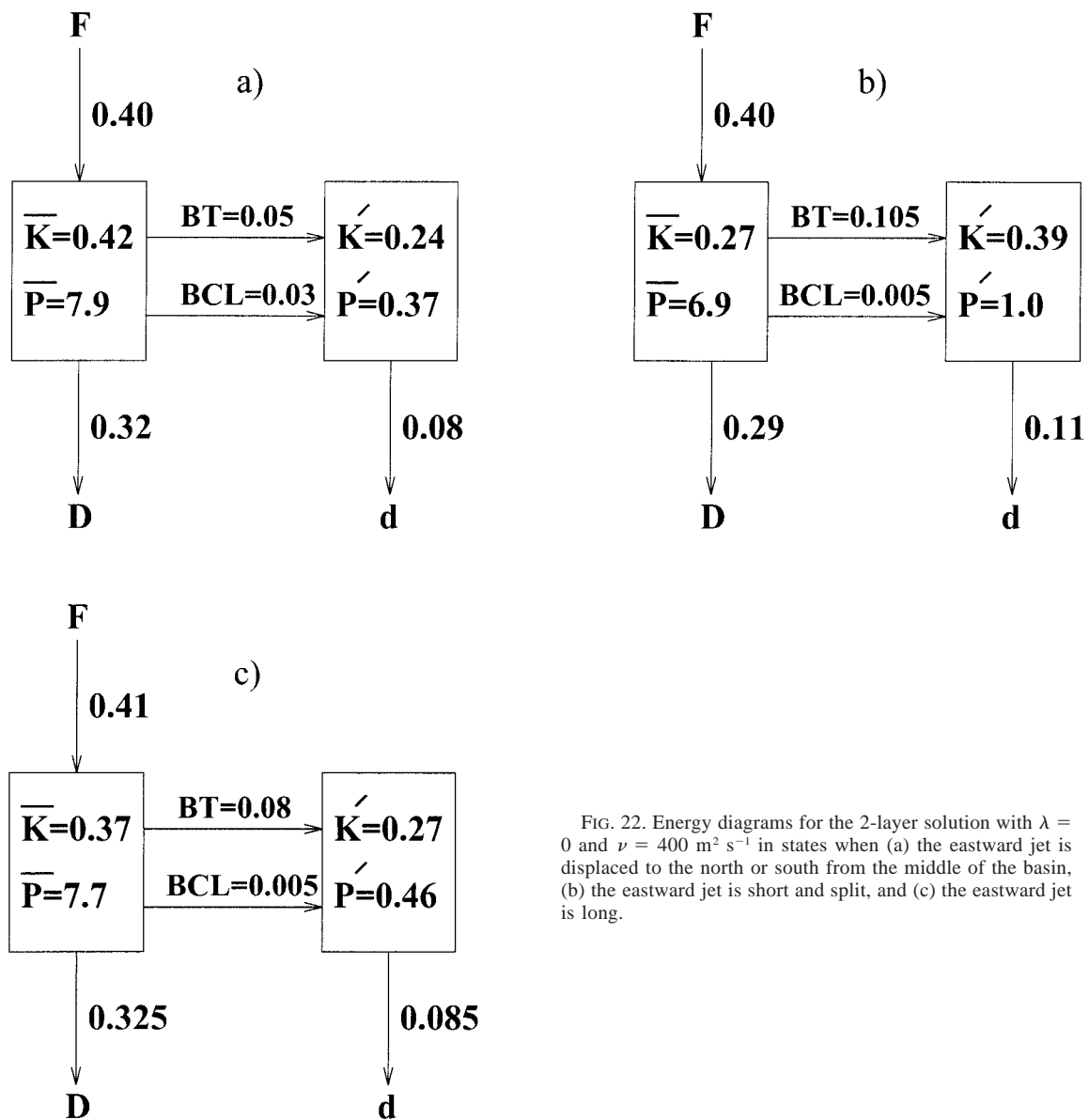


FIG. 22. Energy diagrams for the 2-layer solution with  $\lambda = 0$  and  $\nu = 400 \text{ m}^2 \text{ s}^{-1}$  in states when (a) the eastward jet is displaced to the north or south from the middle of the basin, (b) the eastward jet is short and split, and (c) the eastward jet is long.

eastward jet is more intense and penetrates farther to the east; the separation point retreats closer to the middle of the basin. The jet exhibits strong meandering and subsequent eddy detachment and shedding. The quasi-annual band in the spectrum is less prominent, and the interannual power increases with  $Re$ . Again, the LF variability is associated with north-south shifts of the jet and recirculation zones and changes in their intensity. The centers of these fluctuation patterns are shifted away from the western boundary along with the mean jet. The LF statistical distribution has only a slightly higher probability of the anomalous high and low energy events than a normal distribution. For smaller  $R_d$  there is a regime transition when the western boundary current

becomes locally unstable. We explore this in Berloff and McWilliams (1998).

In the symmetrically forced 1.5- and 2-layer solutions the primary mode has a very small amplitude. Thus, contrary to the asymmetric case, the secondary mode completely dominates the variability at intermediate  $Re$ , and it is associated with large variations of the potential energy due to its large spatial scale. At high  $Re$  the LF variability has both very long timescales (decade and longer) and large amplitudes. It is very different from the asymmetric regime. The dominant pattern is associated with relatively slow growth and quick destruction of the intense recirculation zones surrounding the eastward jet. This LF pattern evolves from the secondary

mode as  $Re$  increases. The statistical distributions in the 1.5-layer solution have large deviations from a normal distribution. This is similar to the behavior shown in McCalpin and Haidvogel (1997). In the 2-layer model the LF cycle is stabilized substantially due to baroclinic instability in the recirculation zones, and the fluctuation timescale and amplitude are both smaller. The LF variability pattern is associated with changes in the eastward jet and recirculation zones, as in the asymmetric case, but the intervals with a disrupted jet are much longer and correspond to large drops in energy. During such intervals the flow contains two well-separated, meandering jets. In the opposite intervals with a single, well-formed eastward jet, the gyre pattern is asymmetric in spite of the symmetric forcing with the jet axis displaced either north or south of the middle of the basin. The transitions from one asymmetric state to its mirror image are less frequent in the 2-layer solutions than in 1.5-layer solutions, and the time between them is typically equal to several growth and destruction cycles.

Among the different cases examined here, it seems likely that the dynamical behavior of the 2-layer, asymmetrically forced,  $\nu = 400 \text{ m}^2 \text{ s}^{-1}$  case may be the most relevant one to the real ocean. From the solutions presented here, as well as some precedents in the literature and additional solutions, we have calculated with better resolution and larger  $Re$ , we conclude that broadband, large-scale, low-frequency variability is likely to be typical of ocean models with small viscosity, hence likely to occur in the real ocean as well. However, since the models used here are so highly idealized and the LF variability of the ocean is so poorly known, no quantitative prediction about real LF variability is yet warranted until further steps are taken in the model formulation, principally transient forcing, diabatic processes, and complex domain geometry. Nevertheless, in spite of the differences in mean circulation and temporal statistics, there is common LF behavior across the different models we have examined: at large  $Re$  the LF variability is substantial in amplitude, and its spatial pattern is one of changes in the strength and meridional location of the eastward jet and recirculation zones. Since this occurs in the ocean at sites with intense air-sea heat and water flux, the intrinsic variability of gyres may potentially have an important influence on climate.

*Acknowledgments.* Funding for this research was provided by the National Air and Space Agency (NAG 5-3982) and the National Science Foundation (OCE-9633681).

## APPENDIX A

### EOF Analysis

An empirical orthogonal function decomposition is a technique widely used in analyzing geophysical data (Preisendorfer 1988). The main purpose of this method

is to reduce a dataset containing a large number of variables and time records to a smaller dataset representing a large fraction of the spatiotemporal variability contained in the original data. This goal can be achieved if there is substantial correlation among the data variables. In this case, we want to find a few EOFs that are mutually uncorrelated and contain most of the variance in the original data.

The EOF decomposition is performed on the dataset with the time-mean subtracted out (data anomalies). The original data is restored when the time-mean field is added back to the anomalies expressed as the sum of the EOFs. Let us consider a data anomalies set with  $N$  variables and  $M$  time records (e.g., the streamfunction values at  $N$  different locations, and recorded in time intervals  $m$ ):  $\mathbf{f}(\mathbf{x}, \mathbf{m})$ , where the set of locations is  $\mathbf{x} = (\mathbf{x}_1, \mathbf{x}_2, \dots, \mathbf{x}_N)$ ; and there are  $M$  data vectors

$$f^{(m)} = (f(x_1, m), f(x_2, m), \dots, f(x_N, m)).$$

The new vectors, or EOFs, are obtained as the eigenvectors  $\mathbf{E}^{(k)}$  of the covariance matrix  $\mathbf{C}_{ij}$  performed on the original anomalies. The elements of  $\mathbf{C}_{ij}$  are

$$C_{i,j} = \frac{1}{M} \sum_{m=1}^M f(x_i, m)f(x_j, m).$$

The time-dependent amplitude  $A^{(k)}(m)$  for the  $k$ th EOF is obtained as the projection of the data vector  $\mathbf{f}(\mathbf{x}, \mathbf{m})$  on the particular eigenvector  $\mathbf{E}^{(k)}$ :

$$A^{(k)}(m) = \sum_{n=1}^N E_n^{(k)} f_n^{(m)}.$$

The eigenvectors are ordered so that  $\mathbf{E}^{(1)}$  has the largest eigenvalue  $\lambda_1$ , and the other eigenvectors are numbered in order of decreasing eigenvalue:  $\lambda_{i+1} \leq \lambda_i$ . The variance of the  $k$ th EOF is the  $k$ th eigenvalue  $\lambda_k$ . We truncate the eigenvector sequence so that it contains more than 97% of the variance.

Starting with some arbitrary initial conditions, we spin up the model for a time varying from  $10^4$  to  $5 \times 10^4$  days. Then we run the model for about  $10^5$  days and save the data for the EOF analysis. In addition, we split the data in two equally long records and analyze each of them separately in order to see that the EOFs, energetics, and the time-average fields are robust.

The data are sampled in all layers on an equally spaced  $65 \times 65$  grid. The data vector elements are  $\psi_{1,2}(x_i, x_j)$  as the main choice and  $\mathbf{ud}\psi_{1,2}(x_i, x_j)$  as the auxiliary choice. Around certain frequency bands the data are temporally filtered by a nonrecursive 201-point filter (Otnes and Enochson 1978). Since EOF decomposition is not unique with respect to the choice of the original data elements, the main and auxiliary EOF sets are compared in order to separate robust patterns and their characteristics from decomposition-dependent details.

## APPENDIX B

## Energetics

The dynamics of certain regimes of the spatiotemporal variability can be partially revealed by the energy balance in the flow. If the solution in terms of the streamfunction is decomposed into the time-mean  $\Psi_{1,2}(x, y)$  and perturbations  $\psi'_{1,2}(x, y, t)$ , then the energy density of the mean state is

$$E(x, y) = \sum_{i=1,2} \frac{H_i}{H} \frac{|\nabla \Psi_i|^2}{2} + \frac{S_{1,2}H_1 + S_{2,1}H_2}{4(H_1 + H_2)} (\Psi_1 - \Psi_2)^2 dx dy, \quad (\text{B1})$$

and the perturbation energy density is

$$E'(x, y) = \sum_{i=1,2} \frac{H_i}{H} \frac{|\nabla \psi'_i|^2}{2} + \frac{S_{1,2}H_1 + S_{2,1}H_2}{4(H_1 + H_2)} (\psi'_1 - \psi'_2)^2 dx dy. \quad (\text{B2})$$

Equations governing the energy evolution are

$$\frac{\partial E}{\partial t} = 0 = \nabla \cdot \mathbf{M} - P - R - \frac{H_1}{H} \Psi_1 \nabla \times \tau - \nu \sum_{i=1,2} \frac{H_i}{H} (\nabla^2 \Psi_i)^2 \quad (\text{B3a})$$

$$\left\langle \frac{\partial E'}{\partial t} \right\rangle = \nabla \cdot \mathbf{m} + P + R - \nu \sum_{i=1,2} \frac{H_i}{H} \langle (\nabla^2 \psi'_i)^2 \rangle, \quad (\text{B3b})$$

where angle brackets denote full or conditional time-average, the energy density conversion (exchange) rates between the time-mean flow and perturbations are

$$P(x, y) = - \sum_{i=1,2} \frac{H_i}{H} \langle \psi'_{ix} J(\psi'_i, \Psi_{ix}) + \psi'_{iy} J(\psi'_i, \Psi_{iy}) \rangle \quad (\text{B4a})$$

$$R(x, y) = - \frac{S_{1,2}H_1 + S_{2,1}H_2}{2H} \times \langle (\psi'_1 - \psi'_2) J([\psi'_1 + \psi'_2], \Psi_1 - \Psi_2) \rangle, \quad (\text{B4b})$$

$\mathbf{M}$  and  $\mathbf{m}$  are the energy fluxes, and  $H = H_1 + H_2$  is the total depth. Here  $P$  is the energy exchange between the mean state and perturbations due to the work done by horizontal Reynolds stress;  $R$  is the energy exchange due to the work done by isopycnal form stress associated with divergence of the heat flux of the fluctuations. The so-called barotropic instability (i.e., extracting fluctuation energy from the mean horizontal shear) is associated with a positive basin integral of  $P$ , and baroclinic instability (i.e., extracting fluctuation energy from the mean vertical shear or horizontal temperature gradient) corresponds to a positive basin integral of  $R$  (Pedlosky 1987). The spatial distributions of  $P$  and  $R$  give a rough idea of the parts of the flow that are most significant in the energy conversions.

Given  $P(x, y)$  and  $R(x, y)$ , the energy conversion rates averaged over the basin area are

$$\text{BT} = \frac{1}{A} \iint_A P(x, y) dx dy \quad (\text{B5a})$$

$$\text{BCL} = \frac{1}{A} \iint_A R(x, y) dx dy, \quad (\text{B5b})$$

the rate of external forcing of the mean by the wind curl is

$$F = - \frac{H_1}{AH} \iint_A \Psi_1 \nabla \times \tau dx dy, \quad (\text{B5c})$$

the rate of the mean energy dissipation is

$$D = - \frac{\nu}{A} \iint_A \sum_{i=1,2} \frac{H_i}{H} (\nabla^2 \Psi_i)^2 dx dy, \quad (\text{B5d})$$

and the rate of the perturbation energy dissipation is

$$d = - \frac{\nu}{A} \iint_A \sum_{i=1,2} \frac{H_i}{H} \langle (\nabla^2 \psi'_i)^2 \rangle dx dy. \quad (\text{B5e})$$

The basin averages of the forcing, conversion, and dissipation rates are used in the energy diagrams in Figs. 9, 13, and 22. The basin averages of the flux divergence terms are equal to zero due to the boundary conditions (4) and (5), but the term  $\langle \partial E' / \partial t \rangle$  and its basin average are not necessarily zero when the time-averaging is taken conditionally over certain intervals of time. In our case this term gives very small corrections, less than 0.5%, to the basin averaged energy balances, therefore we do not show it in the energy diagrams.

## REFERENCES

- Barnier, B., B. Hua, and C. Le Provost, 1991: On the catalytic role of high baroclinic modes in eddy-driven large-scale circulations. *J. Phys. Oceanogr.*, **21**, 976–997.
- Berloff, P., and S. Meacham, 1997: The dynamics of an equivalent-barotropic model of the wind-driven circulation. *J. Mar. Res.*, **55**, 523–563.
- , and —, 1998: The dynamics of a simple baroclinic model of the wind-driven circulation. *J. Phys. Oceanogr.*, **28**, 361–388.
- , and J. McWilliams, 1999: Quasigeostrophic dynamics of the western boundary current. *J. Phys. Oceanogr.*, in press.
- Cessi, P., 1991: Laminar separation of colliding western boundary currents. *J. Mar. Res.*, **49**, 697–717.
- , and G. Ierley, 1995: Symmetry-breaking multiple equilibria in quasigeostrophic wind-driven flows. *J. Phys. Oceanogr.*, **25**, 1196–1205.
- Constantin, P., C. Foias, B. Nicolaenko, and R. Temam, 1989: *Integral Manifolds and Inertial Manifolds for Dissipative Partial Differential Equations*. Springer-Verlag, 122 pp.
- Dijkstra, H., and C. Katsman, 1997: Temporal variability of the quasigeostrophic wind-driven double-gyre ocean circulation: Basic bifurcation diagrams. *Geophys. Astrophys. Fluid Dyn.*, **85**, 195–232.
- Drazin, P., 1992: *Nonlinear Systems*. Cambridge University Press, 317 pp.
- Guckenheimer, J., and G. Buzyna, 1983: Dimension measurements for geostrophic turbulence. *Phys. Rev. Lett.*, **51**, 1438–1441.
- Haidvogel, D., and W. Holland, 1978: The stability of ocean currents

- in eddy-resolving general circulation models. *J. Phys. Oceanogr.*, **8**, 393–413.
- , J. McWilliams, and P. Gent, 1992: Boundary current separation in a quasi-geostrophic, eddy-resolving ocean circulation model. *J. Phys. Oceanogr.*, **22**, 882–902.
- Harrison, D., and S. Stalos, 1982: On the wind-driven ocean circulation. *J. Mar. Res.*, **40**, 773–791.
- Holland, W., 1978: The role of mesoscale eddies in the general circulation of the ocean—Numerical experiments using a wind-driven quasigeostrophic model. *J. Phys. Oceanogr.*, **8**, 363–392.
- Holton, J., 1992: *An Introduction to Dynamic Meteorology*. 3d ed. Academic Press, 511 pp.
- Jiang, S., F. Jin, and M. Ghil, 1995: Multiple equilibria, periodic, and aperiodic solutions in a wind-driven, double-gyre, shallow-water model. *J. Phys. Oceanogr.*, **25**, 764–786.
- LeProvost, C., and J. Verron, 1987: Wind-driven ocean circulation transition to barotropic instability. *Dyn. Atmos. Oceans*, **11**, 175–201.
- Lions, J.-L., R. Temam, and S. Wang, 1992: On the equations of the large-scale ocean. *Nonlinearity*, **5**, 1007–1053.
- Marshall, J., and G. Shutts, 1981: A note on rotational and divergent eddy fluxes. *J. Phys. Oceanogr.*, **11**, 1677–1680.
- McCalpin, J., and D. Haidvogel, 1997: Phenomenology of the low-frequency variability in a reduced-gravity, quasigeostrophic double-gyre model. *J. Phys. Oceanogr.*, **27**, 739–752.
- McWilliams, J., 1977: A note on a consistent quasi-geostrophic model in a multiply connected domain. *Dyn. Atmos. Oceans*, **1**, 427–441.
- , and J. Chow, 1981: Equilibrium geostrophic turbulence I: A reference solution in a  $\beta$ -plane channel. *J. Phys. Oceanogr.*, **11**, 921–949.
- , N. Norton, and P. Gent, 1990: A linear balance model of wind-driven, midlatitude ocean circulation. *J. Phys. Oceanogr.*, **20**, 1349–1378.
- Meacham, S., and P. Berloff, 1997a: Barotropic, wind-driven circulation in a small basin. *J. Mar. Res.*, **55**, 407–451.
- , and —, 1997b: Instabilities of a steady, barotropic, wind-driven circulation. *J. Mar. Res.*, **55**, 885–913.
- Moro, B., 1988: On the non-linear Munk model. I: Steady flows. *Dyn. Atmos. Oceans*, **12**, 259–287.
- , 1990: On the non-linear Munk model. II: Stability. *Dyn. Atmos. Oceans*, **14**, 203–227.
- Otnes, R., and L. Enochson, 1978: *Applied Time Series Analysis*. Vol. 1. Wiley and Sons, 449 pp.
- Pedlosky, J., 1987: *Geophysical Fluid Dynamics*. 2d ed. Springer-Verlag, 710 pp.
- Preisendorfer, R., 1988: *Principal Component Analysis in Meteorology and Oceanography*. Elsevier, 425 pp.
- Primeau, F., 1998: Multiple equilibria of a double-gyre ocean model with super-slip boundary conditions. *J. Phys. Oceanogr.*, **28**, 2130–2147.
- Sheremet, V., G. Ierley, and V. Kamenkovich, 1997: Eigenanalysis of the two-dimensional wind-driven ocean circulation problem. *J. Mar. Res.*, **55**, 57–92.
- Speich, S., H. Dijkstra, and M. Ghil, 1995: Successive bifurcations in a shallow-water model applied to the wind-driven ocean circulation. *Nonlin. Proc. Geophys.*, **2**, 241–268.
- Verron, J., and C. Le Provost, 1991: Response of eddy-resolved general circulation numerical models to asymmetrical wind forcing. *Dyn. Atmos. Oceans*, **15**, 505–533.
- , —, and W. Holland, 1987: On the effects of a midocean ridge on the general circulation: Numerical simulations with an eddy-resolved ocean model. *J. Phys. Oceanogr.*, **17**, 301–312.